Appendix A

List of attached animation files

The DVD attached to this thesis contains several animations of calculated results in .avi format for viewing on most computer operating systems. The animation files included are

wetzel2000-temp.avi A plate with applied temperature gradient in an intense acoustic field. Working fluid is air at atmospheric pressure. Video is a plot of temperature contours, and shows the development of vortices on plate edges. The vortices actually improve the effectiveness of heat transfer between the solid and the gas. Sound pressure level modelled is ’only’ 154dB, with f=100Hz. To be viewed in conjunction with the study presented in Appendix D.2.

4pk-templeft-1.7.avi This model considers four plates in an axisymmetric representation of a resonator from Run 3 of Chapter 6. The upper boundary is a solid wall, the lower boundary is a symmetric condition representing the pipe centre axis. f=100Hz, helium at 1 atm, drive ratio DR of 1.7%. The cooling of the gas at certain phases in the cycle can be seen. This model gives greater insight into acoustic streaming (time-averaged non-zero flow) which is a significant loss mechanism in modern thermoacoustic devices.

4pk-tempright-1.7.avi The same simulation as 4pk-templeft-1.7.avi, but at the right-hand or ‘hot’ end.

4pk-pathleft-1.7.avi Pathlines for Run 3 of Chapter 6 at the left (‘cold’) end of the stack region.

4pk-pathright-3.4.avi Pathlines for Run 4 of Chapter 6 at the right (‘hot’) end of the stack region. Frames in this animation correspond to those presented on the right hand side of Figures 6.5 and 6.6.

edge-talon-pathleft-1.7.avi Pathlines are generated over an oscillatory cycle for the left end of the Talon edge profile at a drive ratio is 1.7% (Run 4 of Chapter 5).

edge-round-velleft-1.7.avi Velocity vectors over the left end of the Rounded edge model at a drive ratio of 1.7% (Run 2 of Chapter 5). To be viewed in conjunction with the study presented in Chapter 5.

Appendix B

Selection of numerical model parameters

Section B.1 provides background on the CFD environment. Sections B.2, B.3 and B.4 present studies used to select suitable settings for turbulent solver model, grid mesh density and timestep size respectively.

B.1 Computational environment

Each model is constructed and evaluated using the commercial CFD software *Gambit* and *Fluent* (*FLUENT 6.2.16 User Manual* 2006), specifically utilising the two-dimensional double-precision ('2ddp') environments.

The thermoacoustic couple is 'driven' using what is termed a 'pressure inlet' boundary condition, in which an oscillatory pressure is specified (based upon the flow-time) at the leftmost boundary of the model. In the case of reverse flow (mass flow entering the left hand side of the domain), the temperature of the incoming fluid is set equal to the ambient initial temperature (e.g. 300K). Since under this condition, incoming fluid to the domain is at a different temperature to fluid in the vicinity of the stack region, the pressure inlet boundary is set at distance L_A

from the stack region as shown in Figure 3.1. At the lower drive ratios, L_A is many times the gas displacement amplitude $|\xi_1|$, but at the highest drive ratio tested (DR=8.5%), $L_A \approx 1.4|\xi_1|$.

Besnoin (2001, Section 4.2.3) found "sustained drift", or time-averaged change, in normalised flow states at higher drive ratios, despite intelligent iterative refinements of the computational mesh to advance the solution as far as possible. To "overcome the difficulties" of this, Besnoin proposes a more suitable method in which the drive ratio (input acoustic pressure) is explicitly imposed and the velocity is calculated. This is shown to address the problem of drift. The method of imposing a fixed oscillatory pressure and calculating velocity and temperature in a time advancement scheme is presented in this thesis. Besnoin (2001, Figure 4.5) showed graphically the temporal evolution of normalised temperature, pressure and density states, although it is unclear how the abscissa "Normalised time" was determined and how it may be scaled to the current study in terms of acoustic cycles.

Figure B.1 presents the evolution of normalised error in system states such as overall system entropy and energy, and gas temperature difference across the stack region. The error in each state is obtained from the 'cycle to cycle' error (Rivera-Alvarez & Chejne 2001) averaged over the previous 100 time steps (one full cycle). Sustained drift is found in the gas temperature difference and to a lesser degree, the system entropy. Physically, this drift would result in continued increase in temperature difference and system entropy, limited only by the imposed boundary conditions.

B.1.1 Turbulence modelling

Modelling of turbulence within the computational environment is discussed in the following section. The dimensionless peak oscillatory Reynolds number for a smooth

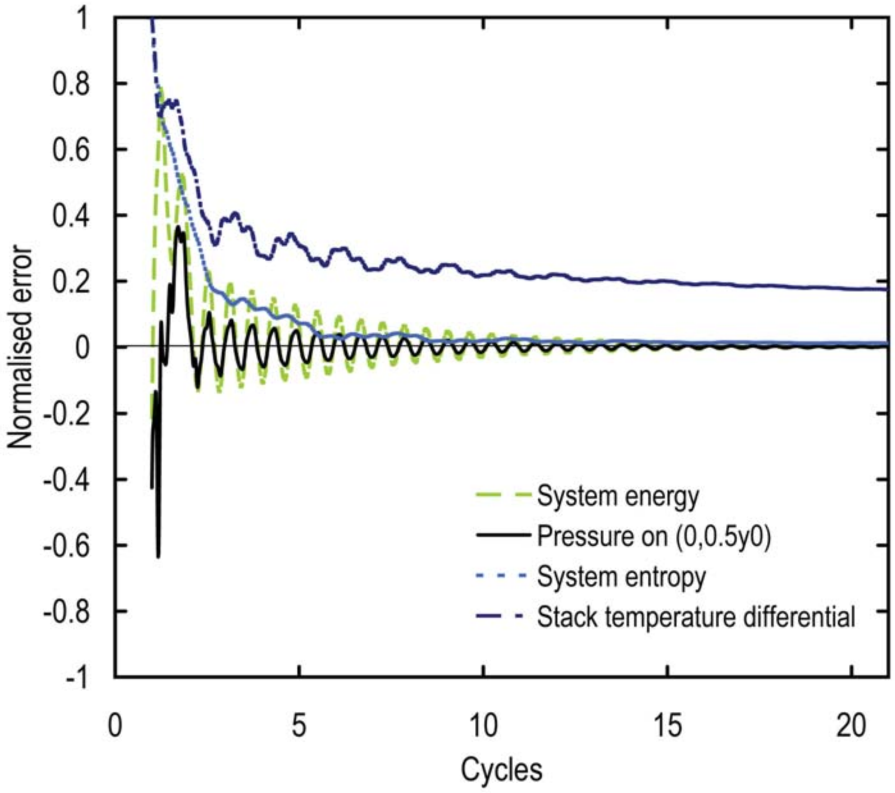

Figure B.1: Normalised error of total system states versus acoustic cycle for Run 1 of Chapter 4. Pressure states are evaluated near the cold side of the stack.

circular pipe is given by (Swift 2002, Equation 7.23)

$$|N_{R,1}| = \frac{|u_1|\, D\rho_m}{\mu}, \tag{B.1}$$

where u_1 is the gas velocity, D is the diameter of the pipe interior, ρ_m is mean gas density and μ is the gas dynamic viscosity, and may give some insight into whether the flow behaviour is turbulent or not within a stack region. Swift (2002, Figure 7.4) suggests that for flow in pipes with smooth walls, laminar flow is achieved for $|N_{R,1}| < 2,000$ and $2(y_0 - t_s)/\delta_v < 10$, where y_0 is the plate half-spacing, t_s is the plate half-thickness, and δ_v is the viscous penetration depth.

As an example, Figure B.2 shows the velocity of fluid for Run 20 of Chapter 4 for a drive ratio of 6.8% and a blockage ratio of 0.7. The maximum velocity amplitude

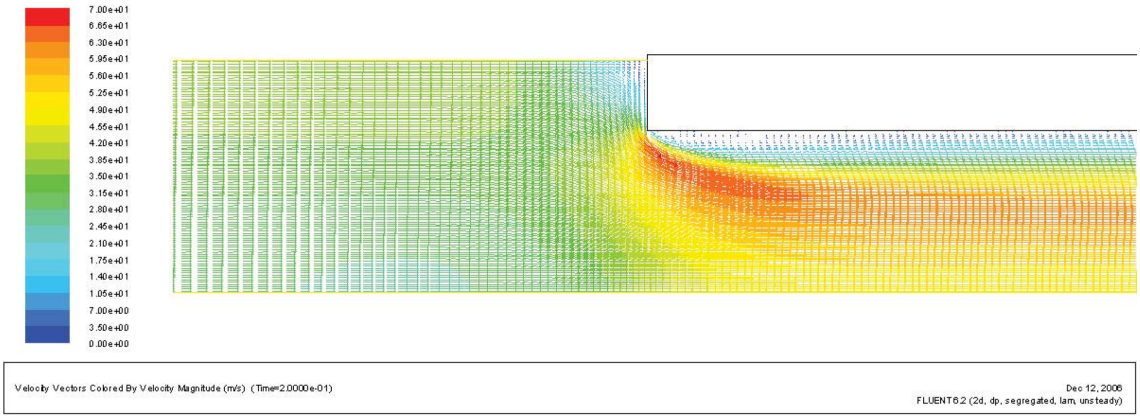

Figure B.2: Velocity magnitude colour vector plot from the *Fluent* CFD environment about the left edge of the thermoacoustic couple simulated in Run 20 of Chapter 4, at t=0.2s. Prevailing flow direction is left to right: contours are shown for the range 0 to 70m/s.

throughout the stack region is $|u_1| \approx 66$m/s. If the stack pore ($2y_0 - 2t_s$=11.2mm) is considered a continuous smooth pipe and entrance / exit effects at the stack pore edges are ignored, Equation (B.1) suggests that the flow is laminar since $|N_{R,1}| \sim 85$. However it will be shown that acoustic streaming and turbulent characteristics do occur at the extremities of the stack region at certain phases in the limit cycle with otherwise laminar behaviour. Merkli & Thomann (1975*a*) refers to similar features in oscillatory pipeflow as "turbulent bursts followed by relaminarisation in the same cycle". The selection of appropriate solution and model properties should enable good time and spatial resolution of such events.

Practical thermoacoustic devices at high drive ratios and power densities do indeed exhibit semi-turbulent or fully turbulent flow at various locations within the device (Swift 2002, Sun et al. 2005), particularly in narrow constrictions or branch connections. Specific criteria for the existence of turbulence within closed channels are less reliable in the stack regions in practical examples because of the relatively minuscule scales involved. Swift (2002, Section 7.2) acknowledges that application of limits using $|N_{R,1}|$ given by Equation (B.1) "significantly underestimate" the transition value for laminar to turbulent flows. For example, the highly tortuous paths of fluid oscillating within a screen bed regenerator would strongly suggest a turbulent mixing action, however Swift notes that such regenerators would typically achieve $|N_{R,1}| \sim 500$. Swift comments that the flow regimes in high-amplitude standing-wave stacks border on the weakly turbulent or conditionally turbulent.

Analyses of the thermoacoustic couple are conducted in this thesis that involve varying the drive-ratio and hence volume velocity of the working fluid to investigate effects such as heat transfer effectiveness or stack performance. However, this variation in flow velocity may lead to two different flow regimes being captured by the same solution model. To address the potential for a weakly-turbulent or conditionally turbulent flow, several configurations of different flow transport models were compared to determine a suitable 'solver profile', or settings which provided an acceptable balance of computational effort, ease of implementation and solution accuracy.

B.1.1.1 The laminar flow model

The majority of computational studies presented in this thesis make use of equations of mass and without near wall corrections at the interface 'WALL' as shown in Figure 4.2.

The equations for continuity and momentum used are (*FLUENT 6.2.16 User Manual* 2006, Section 9.2)

$$\frac{\partial \rho}{\partial t} + \nabla \cdot (\rho \vec{u}) = 0 \tag{B.2}$$

and

$$\frac{\partial \rho}{\partial t}(\rho \vec{u}) + \rho \vec{u} \cdot \nabla \vec{u} = -\nabla p + \nabla \cdot \bar{\bar{\tau}} + \vec{F} \tag{B.3}$$

where ρ is the fluid density, $\vec{u}$ is the velocity vector, p is static pressure, $\vec{F}$ represents external forces and

$$\bar{\bar{\tau}} = \mu \left[(\nabla \vec{u} + \nabla \vec{u}^T - \frac{2}{3} \nabla \cdot \vec{u} I \right] \tag{B.4}$$

is the 'stress tensor' which represents viscous forces. In Equation (B.4), μ is the dynamic viscosity and I is a unit tensor.

In Section 4.1.3.1 it has been determined that use of these equations would be sufficient for flows in thermoacoustic couples where the critical streaming Reynolds number $N_{R,S}$ defined in Equation (4.11) is less than $(200)^2$.

B.1.1.2 Spalart-Allmaras turbulence model

The Spalart-Allmaras (S-A) model is a 'one-equation' turbulence model that was initially developed for aerospace applications involving wall-bounded flows and is popular because of its relative ease of use compared to the classical 'two equation' models such as the k-ϵ or k-ω models (Fares & Schroder 2004). The S-A model is the only turbulence model within the version 6.2.16 *Fluent* environment to contain one turbulent transport equation (*FLUENT 6.2.16 User Manual* 2006) despite the apparent accuracy advantages offered by the more recent 'one-equation' turbulence model developed by Fares & Schroder.

The S-A model accounts for the Reynolds stress term $-(\rho \bar{u}'_i \bar{u}'_j)$ in Equation (B.3) by using the Boussinesq approximation (*FLUENT 6.2.16 User Manual* 2006, Section 11.2.3)

$$-\rho \overline{u'_i u'_j} = \mu_t \left(\frac{\partial u_i}{\partial x_j} + \frac{\partial u_j}{\partial x_i} \right) - \frac{2}{3} \left(\rho k + \mu_t \frac{\partial u_i}{\partial x_i} \right) \delta_{ij}. \tag{B.5}$$

Essentially, use of this approximation leads to modelling of the Reynolds stress tensor as proportional to the mean strain rate, i.e. the momentum transfer of turbulent eddies in the flow can be modelled using the eddy viscosity.

The turbulent viscosity ratio μ_t/μ was set to 5, which is considered reasonable for low Reynolds number flows (*FLUENT 6.2.16 User Manual* 2006, Section 7.2.2). More complex and computationally expensive turbulent models within *Fluent* were not considered on the basis that the flow field at the stack walls would be directly resolved via sufficiently fine meshing and time step iteration and at worst would be conditionally turbulent.

B.1.1.3 Reynolds stress model

A detailed investigation of localised turbulence in thermoacoustic couples described here made use of the Reynolds Stress Transport Equations, also referred to collectively as the Reynolds Stress Model (RSM). It is by far the most computationally expensive of the viscous models discussed here.

In the commercial code *Fluent*, convective heat transfer within the RSM is achieved using (*FLUENT 6.2.16 User Manual* 2006, Section 11.6.9)

$$\frac{\partial}{\partial t}(\rho E) + \frac{\partial}{\partial x_i}\left[u_i(\rho E + p)\right] = \frac{\partial}{\partial x_j}\left[\left(k + \frac{c_p \mu_t}{\sigma_{\mathrm{t}}}\right)\frac{\partial T}{\partial x_j} + u_i(\tau_{ij})_{\mathrm{eff}}\right] \tag{B.6}$$

where E is the total energy, c_p is the thermal capacity, σ_t is the turbulent Prandtl number for energy, $(\tau_{ij})_{\mathrm{eff}}$ is a 'deviatoric' stress tensor and controls the rate of viscous dissipation.

On the basis that the studies presented in this thesis will use an unsteady time formulation, relatively high node counts and many small time steps to model an oscillatory flow structure, the RSM is considered excessive in terms of computational requirement but noted as a viscous solver model worth considering for future simulations where the flow is highly turbulent.

B.1.2 Heat transfer equations

The energy equation in *Fluent* for a homogeneous fluid is given as (*FLUENT 6.2.16 User Manual* 2006, Section 12.2.1)

$$\frac{\partial}{\partial t}(\rho E) + \nabla \cdot (\vec{u}(\rho E + p)) = \nabla \cdot \left(k_{\text{eff}} \nabla T - h\vec{J} + (\bar{\bar{\tau}} \cdot \vec{u})\right) \tag{B.7}$$

where

$$E = h - \frac{p}{\rho} + \frac{u^2}{2} \tag{B.8}$$

and

$$h = \int_{T_{\text{ref}}}^{T} c_p \ dT \tag{B.9}$$

The three components on the right hand side of Equation (B.7) correspond to the energy loss mechanisms of conduction, diffusion and viscous dissipation. The effective thermal conductivity k_{eff} and diffusion flux term J will vary depending on the fluid transport model used. In regions representing solid plate sections, conductive heat transfer is modelled using

$$\frac{\partial}{\partial t}(\rho_s h) + \nabla \cdot (\vec{u}\rho h) = \nabla \cdot (k_s \nabla T) \tag{B.10}$$

where the subscript s refers to properties specific to the solid material modelled.

For evaluation of the sensible enthalpy h, T_{ref} is defined in *Fluent* to be 298.15K (*FLUENT 6.2.16 User Manual* 2006).

B.2 Selection of a suitable solver model

Table B.1 details the solver models considered for use in this study. In the following subsections the implementation of these solver models within the *Fluent* environment will be discussed.

Table B.1: Solver profiles used in this study. Refer to Sections B.1.1.1, B.1.1.2 and B.1.1.3 for specific details regarding the following settings.

Profile	Visc. Model	Discretisation	Wall Approach	Comments
S1	Lam.	1st Ord.	Near-Wall Resol.	Least expensive
S2	Lam.	2nd Ord. Upwind	Near-Wall Resol.	
S3	S-A	2nd Ord. Upwind	Near-Wall Resol.	Single TTE*
S4	RSM	2nd Ord. Upwind	Enhanced	Complex; five TTE*

* turbulent transport equations

The solver profiles can be compared by way of an example to illustrate the accuracy of the results. Figure B.3 presents a comparison of the time-averaged heat flux versus normalised stack position for the solver profiles listed in Table B.1 for a thermoacoustic couple of zero-thickness. It can be seen from this figure that solver profile ‘S2’ is a close match to previously reported results by Piccolo & Pistone (2006) (and therefore also Ishikawa & Mee (2002)), and the result of solver profile ‘S1’ is a close fit to that using ‘S2’. Figure B.3 also shows that as the complexity of the solver is increased, the predicted rate of heat transfer of the couple also increases. It is reasonable to suspect that this increase in time-averaged heat transfer could be attributed to turbulence effects captured by the more complex models.

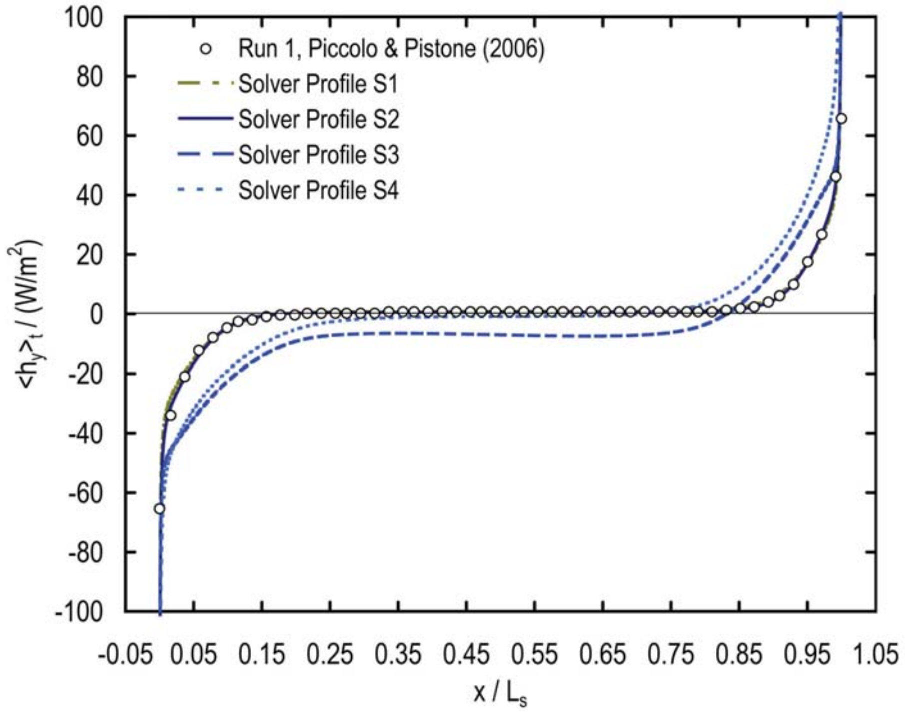

Figure B.3: Time-averaged transverse heat flux versus normalised stack position for selected solver profiles. Modelspace is of a thermoacoustic couple of zero thickness using a 133,000 node mesh. DR of 1.7%.

In selecting a suitable numerical solver model, the computational cost (and hence required timeframes), reasonable level of accuracy and compatibility with previously published work were identified as the most important aspects. In the preliminary study of Chapter 4, solver profile 'S1' was selected to produce results that are in good agreement with previous studies with relatively short solver times. Solver profile 'S1' was selected also on the basis of reduced computational resources available at the time. Chapters 5 and 6 use the solver profile 'S2' to produce results of higher accuracy and repeatability.

B.3 Selection of a suitable grid sizing profile

As the computational resources available to researchers increases, numerical simulations of increasingly complex geometry become more cost effective. A useful indicator of the mesh density of a thermoacoustic couple is the ratio of the thermal penetration depth δ_κ to the size of each grid cell in the vicinity of the stack surface. Previous numerical studies have used grid mesh sizings of typically $\delta_\kappa/15$ (Piccolo & Pistone 2006) to $\delta_\kappa/10$ (Marx & Blanc-Benon 2005*b*).

Table B.2 presents a comparison of typical axial and lateral grid spacings used in modelling thermoacoustic couples. All studies presented in Table B.2 use a quadrilateral mesh. This is preferable since the mesh is aligned with the prevailing flow, minimising the level of numerical diffusion in the solution (*FLUENT 6.2.16 User Manual* 2006, Section 6.1.3). As can be seen from the table, the studies presented in Chapters 4, 5 and 6 utilise a mesh density equal to or higher than comparable studies of thermoacoustic couples.

Table B.2: Comparison of typical axial and lateral grid sizings used in selected numerical studies of thermoacoustic stacks: L_S is the plate length, Δx and Δy are the grid mesh spacings in the x and y directions respectively and $\delta_{\kappa m}$ is the mean thermal penetration depth.

Study	$L_S/\Delta x$	$\delta_{\kappa m}/\Delta y$
Marx & Blanc-Benon (2005*b*)	-	10
Cao et al. (1996)	80	11.5
Ishikawa & Mee (2002)	100	12-24
Piccolo & Pistone (2006)	244	15
Chapter 4, Run 20 (Mesh Profile ‘G2’): ∼33,903 nodes	504	15
Chapter 4, Run 20 but using Mesh Profile ‘G3’: ∼133,200 nodes	1008	30
Section B.3, Case B using Mesh Profile ‘G4’: ∼528,060 nodes	2016	60

B.3.1 Grid mesh profiles

Five different mesh profiles were constructed to explore the grid dependency of the model for the modelspace shown in Figure 3.1 and the mesh density of these profiles is listed in Table B.3. Mesh profile ‘G1’ enables comparison with the results of Piccolo & Pistone (2006), but is considered to have insufficient resolution of models for finite thickness stack plate models.

Table B.3: Comparison of typical axial and lateral grid sizings used in this thesis. Refer to Figure 3.1 for definitions of the grid interval count n. e is the (spatial) ratio used within *Gambit* (*FLUENT 6.2.16 User Manual* 2006) to grade the mesh along each subdomain boundary.

Profile	n_{xS}	n_y	n_{xA}	e_{xA}, e_{xB}	Nodecount	Comments
G1	244	50	32	0.8	~16,859	Lowest resolution
G2	504	50	64	0.8	~33,903	
G3	1008	100	128	0.8	~135,232	
G4	2016	200	256	1.0	~528,060	Highest resolution
G5	504	100	128	1.0	~107,664	Bellshape distrib. of n_{xS} using exponent of 0.8

The mesh profile 'G2' is considered to have a good compromise between minimising the required computational resources and the resolution of the primary physical states of pressure, velocity and temperature. Mesh profile 'G3' simply doubles the mesh density in both x and y directions. Mesh profile 'G4' doubles the mesh density again, providing the highest fidelity of a thermoacoustic couple simulated to date, albeit at the greatest computational cost.

Mesh profile 'G5' was devised to optimise the distribution of nodes for resolution of flow structures at the edges of the stack plates. The results presented in Chapter 4, in agreement with Cao et al. (1996) and Ishikawa & Mee (2002), show that the rate of transverse heat flux between the plate and fluid is concentrated at the plate edges. With knowledge that the time-averaged rate of heat transfer is concentrated at the edges of the plate, the mesh density is decreased in the centre of the plate. On this basis, mesh profile 'G5' is considered to provide comparable or better accuracy to mesh profile 'G3' for heat transfer between the fluid and plate, whilst requiring less computational effort.

Figure B.4 shows the grid meshes for mesh profiles 'G2' to 'G5' listed in Table B.3. It can be seen from Figure B.4(d) that the mesh profile 'G5' has a higher concentration of nodes near the leading edge of the stack plate than profile ‘G4’ despite using nearly 5 times less nodes overall.

Grid adaption routines, which automatically adjust the mesh density in specified locations to meet certain numerical error criteria, are available options within the *Fluent* environment. However these routines were not selected for this study on the basis of ensuring compatibility with the post-processing methods used (see Appendix C). The post-processing methods that were employed here required that mesh symmetry and node spacing was consistent on or adjacent to the fluid-solid interface for each computational run, regardless of operating conditions.

Fluent recommends that for laminar flow regimes, the grid spacing at walls should obey (*FLUENT 6.2.16 User Manual* 2006, Section 6.2.2)

$$\frac{\Delta y}{2}\sqrt{\frac{|\vec{u}_0|}{\upsilon x_{\mathrm{bl}}}} \leq 1 \tag{B.11}$$

where u_0 is the free-stream velocity, and x_{bl} is the distance along the wall from the starting point of the boundary layer, here assumed to be the distance from the leading plate edge x. For example, for Run 21 of Chapter 4 which used mesh profile ‘G1’ and a drive ratio of 1.7%, the left side of Equation (B.11) is 0.87 at x_{bl}=Δx $\approx$1.034mm and approaches 0.055 for $x \to L_S$.

At the limit state, the distribution of time-averaged transverse heat flux is infinite at the extremities of the plate edges (a classic numerical singularity problem), which introduces an error for finite Δx. The effect of this error can be mitigated by dismissing values obtained within a set of finite proximity to the plate edge, say x_{bl}=5Δx. Incorporating this approach, at higher drive ratios Equation (B.11) is largely satisfied for mesh profile ‘G2’ up to a drive

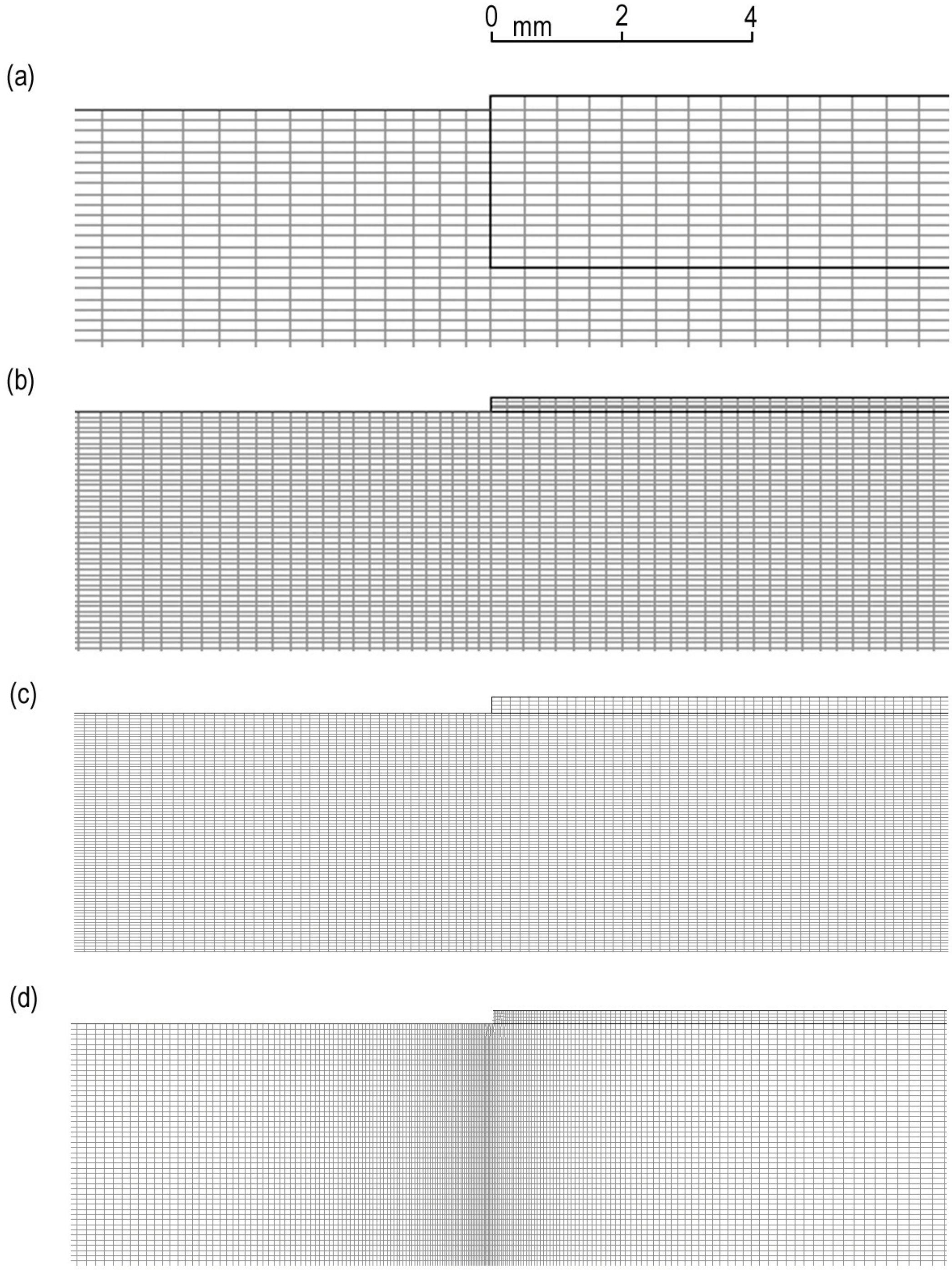

Figure B.4: Close-up view of grid meshes using profiles (a) G2, (b) G3, (c) G4 and (d) G5.

ratio of 8.5%. However, this approach may not be practicable in applications where it is important to resolve the transverse heat flux over the entire plate surface.

For the calculation of effective heat transfer rates and various performance measures, the time-averaged heat flux is weighted using the element face area to remove numerical singularities. In Chapters 5 and 6, this error is considered significant and the condition imposed by Equation (B.11) is achieved for all runs.

B.3.2 Results

Table B.4 lists the error in calculation of the integral of the time-averaged transverse heat flux along the axial plate surface, $\int \left\langle \dot{h}_y \right\rangle_t d\mathrm{A}$, using the result obtained using the finest mesh profile as a best estimate. Solver profile 'S2' was used to model a thermoacoustic couple of thickness t_s=0 at a drive ratio of 1.7% (Case 'A') (*c.f.* Run 1 of Chapter 4) and also t_s=$\delta_{\kappa m}$ $\approx$2.4mm (*c.f.* Run 20 of Chapter 4) at a drive ratio of 6.8% (Case 'B').

Table B.4: Integral of time-averaged transverse heat flux $\int \langle \dot{h}_y \rangle_t d\mathrm{A}$ (W) at limit state for various grid mesh profiles. Case files are otherwise identical to Runs 1 and 20 of Chapter 4. Using the finest grid mesh profile 'G4' as a basis, the comparative error in $\int \left\langle \dot{h}_y \right\rangle_t d\mathrm{A}$ is also provided for each Case.

Case	G1	G2	G3	G4	G5
A (Run 1, Chapt. 4)	1.0530	1.1064	1.2258	1.7948	1.2398
% Error (rel. G4)	-41.3	-38.4	-31.7	-	-30.9
B (Run 20, Chapt. 4)	25.985	26.077	26.868	26.801	26.753
% Error (rel. G4)	-3.05	-2.70	0.25	-	0.18

The time-averaged heat flux versus stack position for each grid profile is presented in Figures B.5 and B.7 for Cases A and B respectively. The result obtained for Case A using grid mesh profile 'G4' deviates from that obtained using other profiles. The discrepancy in the result using 'G4' over results obtained using the other grid mesh profiles can be seen in Figure B.5 as a noticeable increase in effective heat transfer within $\sim 0.2L_S$ of each plate edge. For Case B, Figures B.7 and B.8 show good agreement between results obtained using grid mesh profiles 'G3', 'G4' and 'G5'.

With the highest mesh density, grid mesh profile 'G4' is taken here to be most accurate for the prediction of $\int \langle \dot{h}_y \rangle_t d\mathrm{A}$ and will be used as a comparative basis for accuracy. The result of $\int \langle \dot{h}_y \rangle_t d\mathrm{A}$ using grid profile 'G4' is most closely replicated by grid profiles 'G3' and 'G5', and accuracy to 'G4' indeed scales with increased mesh density.

Figures B.6 and B.8 present the results of Figures B.5 and B.7 for the normalised position x/L_S=0 to 0.15. Case A results (Figure B.6) using 'G1' and 'G2' are near identical, and all results including a previous study using identical operating conditions (Piccolo & Pistone 2006) are in close agreement. The close up of Case B results (Figure B.8) shows the 'G3' and 'G5' results to agree almost perfectly. 'G4' deviates from 'G5' (and 'G3') at approximately x/L_S equal to 0.033: for x/L_S less than 0.0155, profile 'G5' actually has a more dense grid meshing than 'G4', but any expected effects from this are not clear since the differential between 'G5' and 'G4' is greatest within this range.

Table B.5 presents a similar comparison to Table B.4 based on the time-averaged gas temperature difference across the stack region ($\langle \Delta T_{k,hx} \rangle_t$) as defined in Equation (4.12).

Similar comparisons between each grid profile in Table B.4 are found in Table B.5. For Case A, results of $\int \langle \dot{h}_y \rangle_t d\mathrm{A}$ and $\langle \Delta T_{k,hx} \rangle_t$ are both computed to be 19-37% higher using 'G4' than that obtained using any other grid profile. For Case

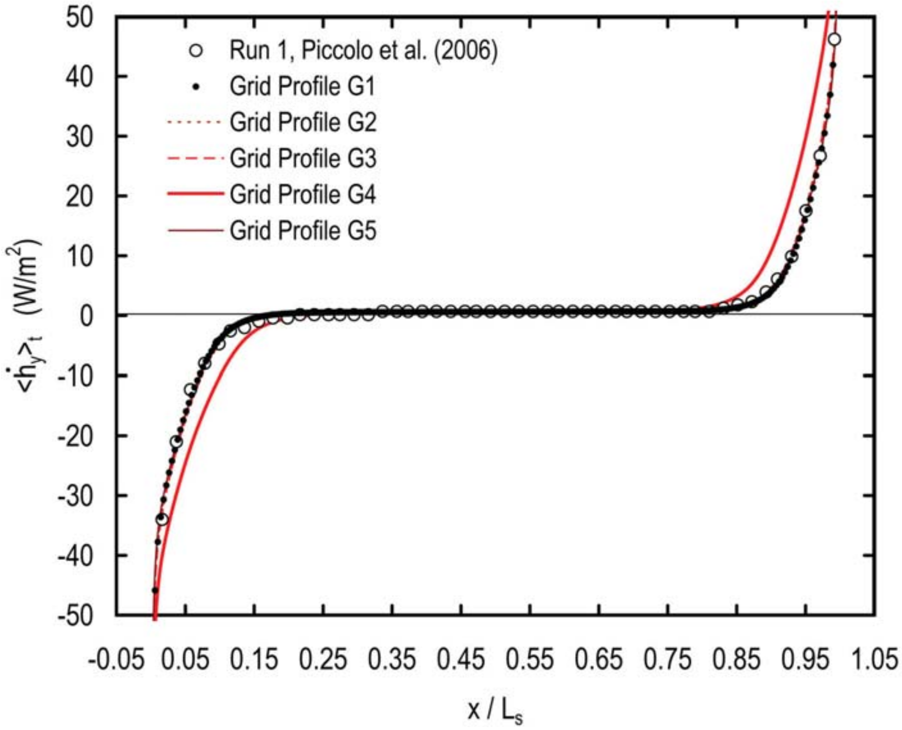

Figure B.5: Normalised stack position x/L_S versus time-averaged transverse heat flux $\left\langle \dot{h}_y \right\rangle_t$ for Case A using selected grid mesh profiles.

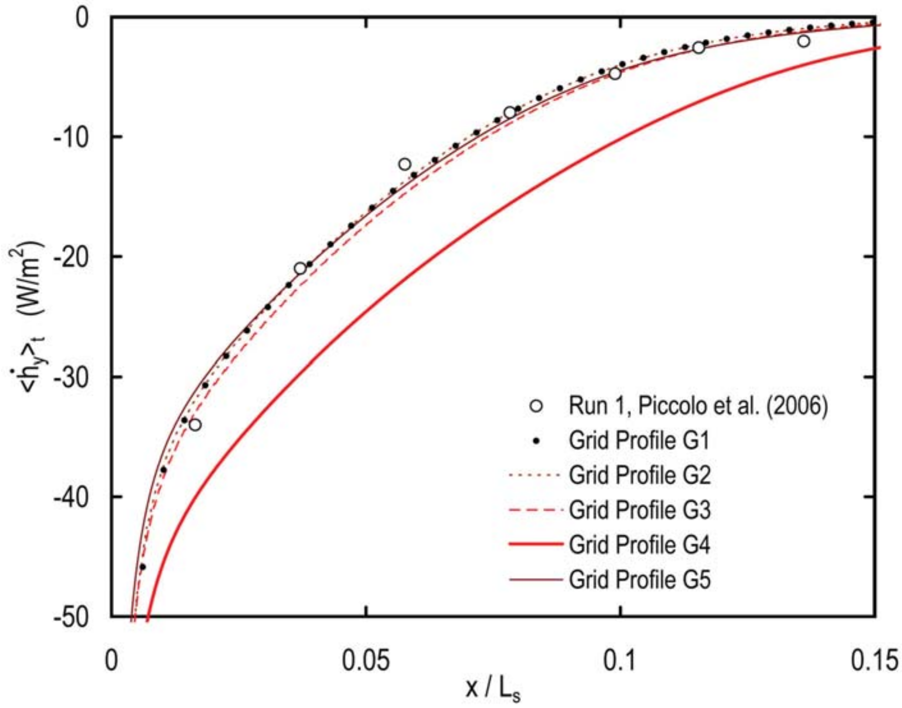

Figure B.6: Close up of Figure B.5 for the range x/L_S=0 to 0.15.

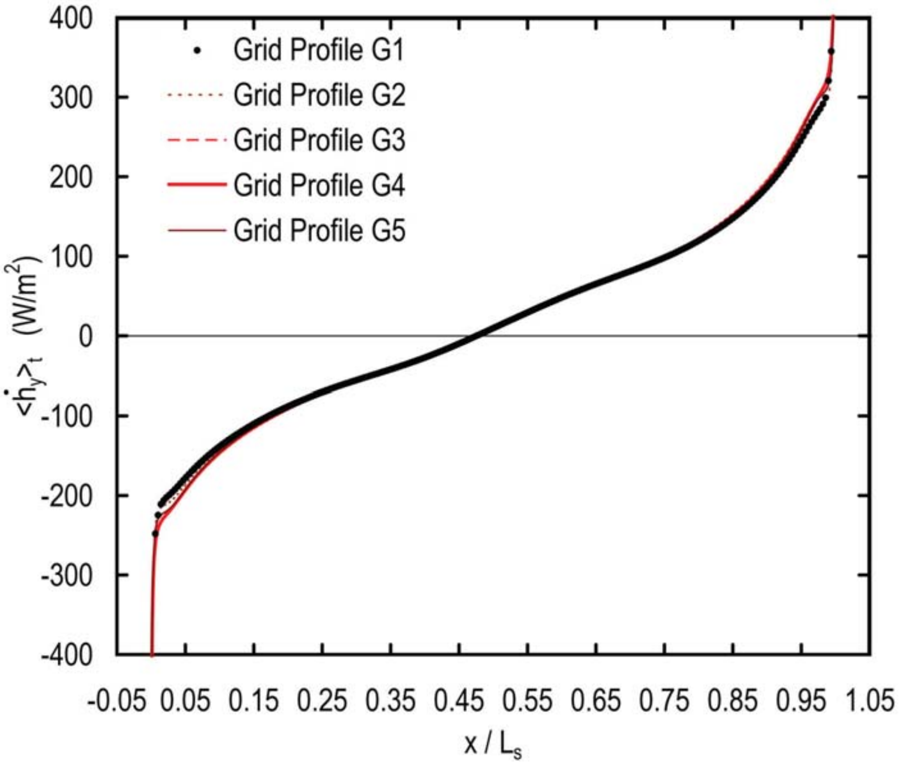

Figure B.7: Normalised stack position x/L_S versus time-averaged transverse heat flux $\left\langle \dot{h}_y \right\rangle_t$ for Case B using selected grid mesh profiles.

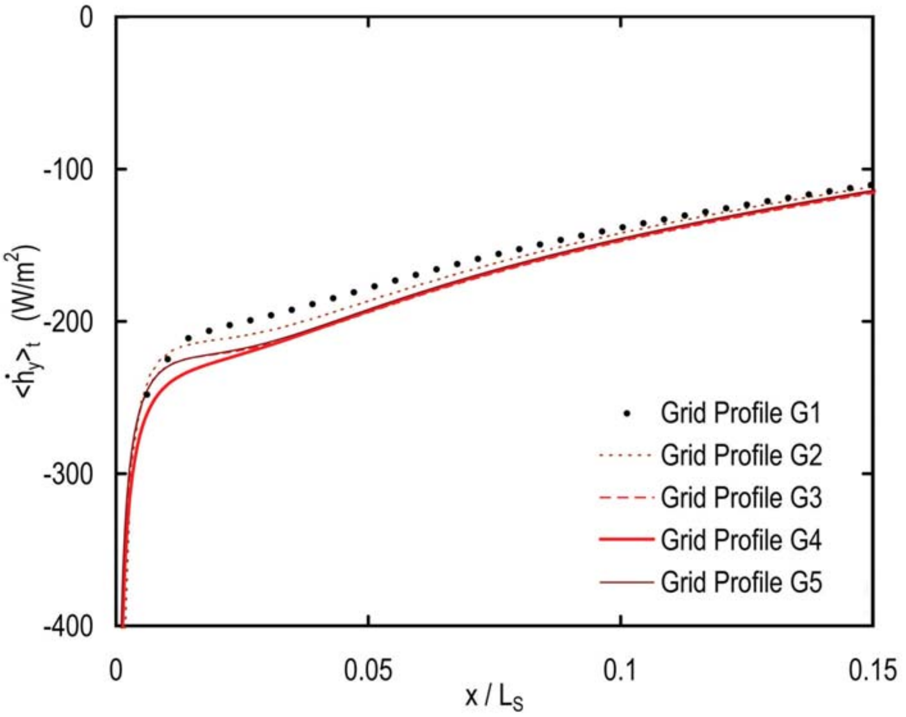

Figure B.8: Close up of Figure B.7 for the range x/L_S=0 to 0.15.

Table B.5: $\langle \Delta T_{k,hx} \rangle_t$ (K) at limit state for various grid mesh profiles. Case files are otherwise identical to Runs 1 and 20 of Chapter 4. Using the highest grid mesh density 'G4' as a basis, the comparative error in $\langle \Delta T_{k,hx} \rangle_t$ is also provided for each case.

Case	G1	G2	G3	G4	G5
A (Run 1, Chapt. 4)	1.489	1.246	1.590	1.975	1.604
% Error (rel. G4)	-24.6	-36.9	-19.5	-	-18.8
B (Run 20, Chapt. 4)	5.450	5.714	6.057	5.866	5.996
% Error (rel. G4)	-7.1	-2.6	3.3	-	2.2

B, both results are only up to 7% different, and profiles 'G3' and 'G5' indeed closely approximate the result using mesh profile 'G4'.

Completion of the studies presented in the following chapters required that the grid profile selected provided a reasonable balance of computational cost and accuracy to previous studies, and ease of implementation. The following studies are centred on models of thermoacoustic couples with finite thickness and drive ratios above 3%, that is, studies closer in form to Case B rather than Case A.

In summary, grid mesh profiles 'G3' and 'G5' are here demonstrated to most closely replicate the results of $\int \langle \dot{h}_y \rangle_t d\mathrm{A}$ and $\langle \Delta T_{k,hx} \rangle_t$ for Case B using the highest grid mesh density considered.

Profile 'G3' is easier to implement than 'G5' as it has a constant grid mesh profile in the stack region, and profile 'G5' is likely to be difficult to implement for curved stack edges. Therefore mesh profile 'G5' will be used where possible (e.g. rectangular stack sections), with 'G3' used for models with complex surface geometry.

B.4 Selection of a suitable timestep size

The segregated implicit solver formulation, as used in the studies presented in Chapters 4 to 6, is unconditionally stable with respect to timescale sizing since time advancement within the model is conditional upon convergence of each term at each time step (*FLUENT 6.2.16 User Manual* 2006, Section 26.2.12). However, it is important to discuss potential error sources encountered in previous numerical studies of thermoacoustic couples, and consider the influence of the time step size Δt upon the simulation results. This is because the performance of the thermoacoustic couple is typically identified over a specific time period and temporal discretisation leads to truncation errors.

Ishikawa (2001) explored the error and convergence rate of several simulations of thermoacoustic couples using an implementation of the software PHOENICS (Spalding 1991) with timescales from 0.83% down to 0.14% of an oscillatory period. Using PHOENICS in single-precision, pressure, velocity and temperature states above a thermoacoustic plate were calculated over as many as 25 full oscillations. With a Courant number of 0.01, Ishikawa found that the rate of convergence of velocity and pressure states increased with increasing time step at the expense of accuracy. Interestingly, the error in calculation of temperature once the simulation had reached limit state was found to increase over time, however Ishikawa acknowledges this may be due to use of SI units in single-precision and associated round-off errors. He concluded that for accuracy requirements of the order of 1%, the computational cost for use of timescales below 0.42% of an oscillatory period was prohibitive.

In consideration of the Courant-Friedrichs-Lewy criterion (Courant et al. 1928), Ishikawa (1999, Equation 4.2) suggests that the timestep

$$\Delta t_{CFL} \leq \frac{1}{(|u|/\Delta x) + (|v|/\Delta y) + a\sqrt{[1/(\Delta x)^2] + [1/(\Delta y)^2]}} \tag{B.12}$$

is required for explicit solving of the two-dimensional Navier Stokes equations where u and v are the components of velocity in the x and y directions. In the x direction of flow, the Courant number (Allison (2006, Equation 1.10)) is given by

$$C = \frac{|\vec{u}_{x,max}|\,\Delta t}{\Delta x} \tag{B.13}$$

where $\vec{u}_{x,max}$ is the resolved maximum velocity in the x direction, and is considered to be strongly linked to the solver numerical accuracy and should be kept at or below 1 (*FLUENT 6.2.16 User Manual* 2006, Section 26.12.1). If an explicit formulation was used, criteria formed from Equations (B.12) and (B.13) would most likely be exceeded at, or slightly downstream of, the stack plate edge using the highest drive-ratio, as highlighted in Figure B.2. In this figure, a $\vec{u}_{max}$ of 66.0m/s is obtained at approximately the point (x,y)=(0,0.00512m), or just 0.48mm from the plate surface at the left edge of the stack region. It is clear that if an explicit solver formulation was used for the same model properties, Equation (B.12) would exceed this requirement at this position with $\Delta t/\Delta t_{CFL} \gg 10^3$, and further refinement of the mesh sizing will only serve to further reduce the recommended timestep size.

B.4.1 Time scale profiles

The study presented in Chapter 4 has a timescale profile of 1%, or in other words, each period is resolved into 100 time steps. Timescales of finer and coarser temporal resolution are considered here to identify their influence on key performance criteria.

The timescale dependency of the model was studied using the timescale profiles listed in Table B.6. Timescale profile 'T0' has the smallest timestep size of 0.1%, but requires 20,000 time steps to be completed by the solver to reach limit state at 0.2s. The timescale of 1% used in Chapter 4 was found to be acceptable in terms of computational cost, and hence only one coarser timescale, 'T4', was considered.

Table B.6: Time profiles used to assess timescale dependency. Timestep (ts) size indicated for an operating frequency f of 100Hz.

Profile	Timescale (%)	ts @ f=100Hz	Comments
T0	0.1	10ns	Finest temporal resolution
T1	0.2	20ns	
T2	0.5	50ns	
T3	1	0.1ms	
T4	2	0.2ms	Coarsest temporal resolution

Similar to the analyses performed for mesh independency (Section B.3), two modelspaces will be used for evaluating the influence of timescale. One modelspace designated Case A has a zero-thickness (blockage ratio of 1) heat exchange surface and a drive-ratio of 1.7%. Case B has a blockage ratio of 0.7 and a drive-ratio of 6.8%. Both modelspaces have the grid mesh profile 'G3' as defined in Table B.3. These case files are otherwise identical to Runs 1 and 20 of Chapter 4.

B.4.2 Results

Table B.7 presents the integral of time-averaged transverse heat flux $\int \left\langle \dot{h}_y \right\rangle_t d\mathrm{A}$ for varying timestep profiles 'T0' to 'T4' of both runs considered. As can be seen from this table, the integral of the transverse heat flux at the internal surface of the heat exchanger increases with increasing time step size.

Figures B.9 and B.10 present the time-averaged transverse heat flux $\left\langle \dot{h}_y \right\rangle_t$ at the 'cold' and 'hot' ends respectively for the various time step sizes used for Case A. At the 'cold end', it can be seen that results from profiles 'T0' and 'T2' are closest in agreement, although all five profiles are reasonably close together, with

Table B.7: Integral of time-averaged transverse heat flux $\int \left\langle \dot{h}_y \right\rangle_t dA$ for various timestep sizes.

Case	T0 (0.1%)	T1 (0.2%)	T2 (0.5%)	T3 (1.0%)	T4 (2.0%)
A (Run 1, Chapt. 4)	4.6957	4.8170	5.0047	5.2056	5.4647
% Error (rel. T0)	-	2.58	6.58	10.8	16.4
B (Run 20, Chapt. 4)	103.63	104.27	104.68	106.62	108.79
% Error (rel. T0)	-	0.62	1.01	2.89	4.98

values of $\left\langle \dot{h}_y \right\rangle_t$ falling within a 10% range regardless of the time profile selected. However, if profile 'T4' is omitted, the grouping is reduced to 8%. At the 'hot end', 'T1' is consistently closest to 'T0'. All values obtained using the five different time profiles typically fall within a 13% range, and omitting 'T4' reduces this range to approximately 10%.

In the midsection of the stack region (defined here to be for $0.15 \leq x/L_S \leq 0.85$) for Case A, Figure B.11 shows $\left\langle \dot{h}_y \right\rangle_t$ to be mainly positive for $x/L_S \geq 0.2$, or over 80% of the surface area. The time-averaged rate of heat flux is predicted to be typically of the order of 0.5W/m^2 in the centre of the stack region using all time step size profiles considered. The simple standard deviation of all five time profiles is typically 0.13W/m^2 in the midsection. The values for $\left\langle \dot{h}_y \right\rangle_t$ obtained using the largest time scale size 'T4' are consistently less than results obtained using other time scales in the midsection of the stack, but are in good agreement elsewhere.

For Case B, Figure B.12 shows $\left\langle \dot{h}_y \right\rangle_t$ for the midsection of the plate. This figure shows that all five timescale profiles appear to be in excellent agreement in this region of the plate, however some deviation can be seen at the extremes of the graph between the coarsest profile 'T4' and the finest profile 'T0'.

Figures B.13 and B.14 present the time-averaged transverse heat flux $\left\langle \dot{h}_y \right\rangle_t$ at the 'cold' and 'hot' ends for various time step sizes used for Case B. Discrepanices

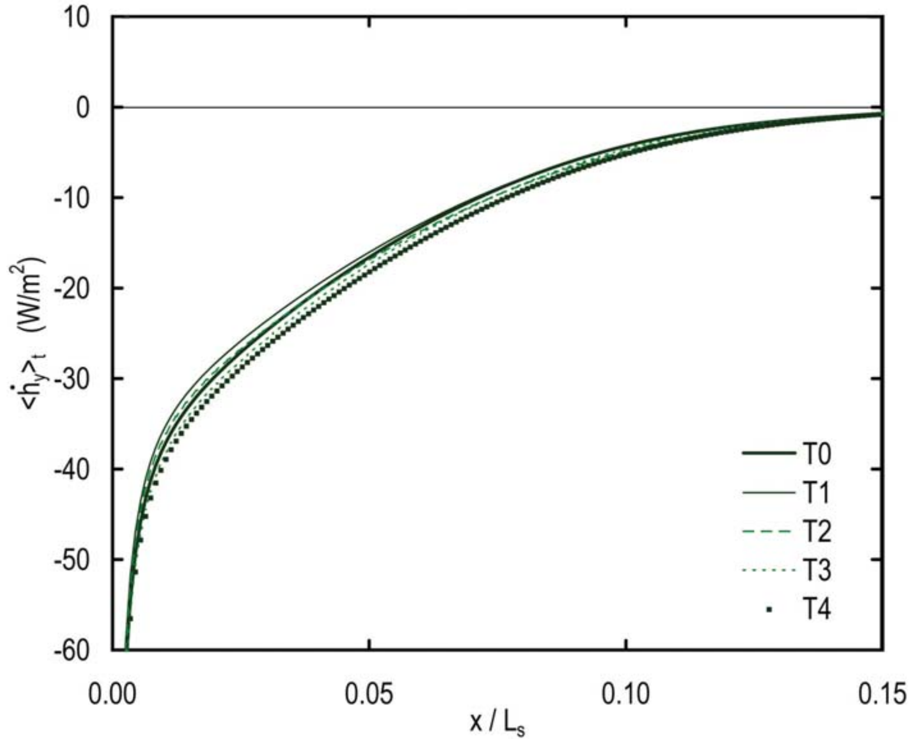

Figure B.9: Normalised stack position x/L_S versus time-averaged transverse heat flux $\left\langle \dot{h}_y \right\rangle_t$ for the stack 'cold end' in Case A using selected timescale profiles.

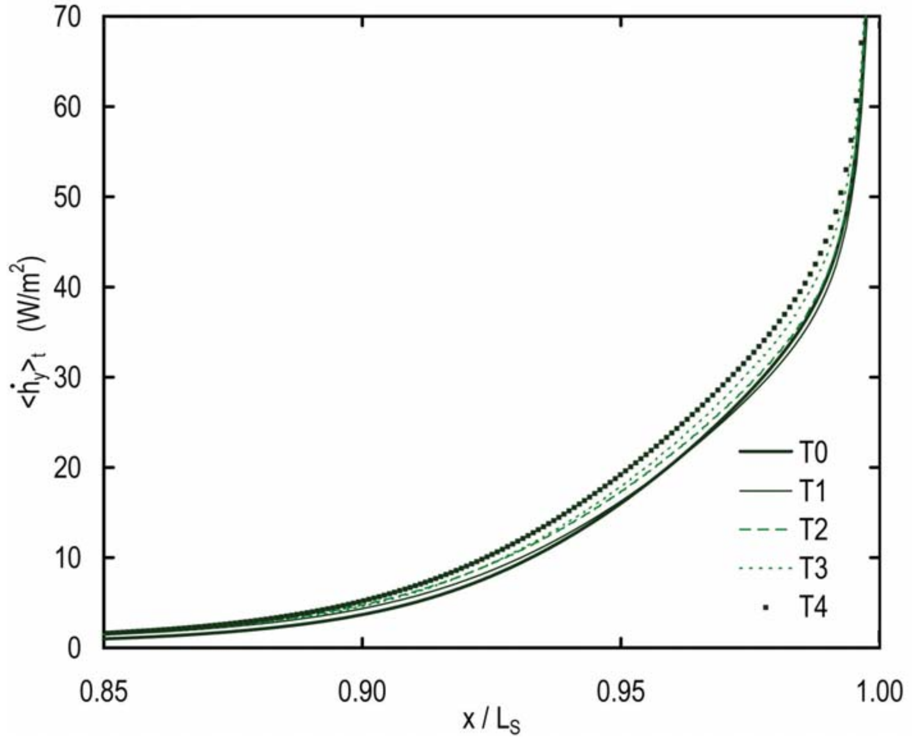

Figure B.10: Normalised stack position x/L_S versus time-averaged transverse heat flux $\left\langle \dot{h}_y \right\rangle_t$ for the stack 'hot end' in Case A using selected timescale profiles.

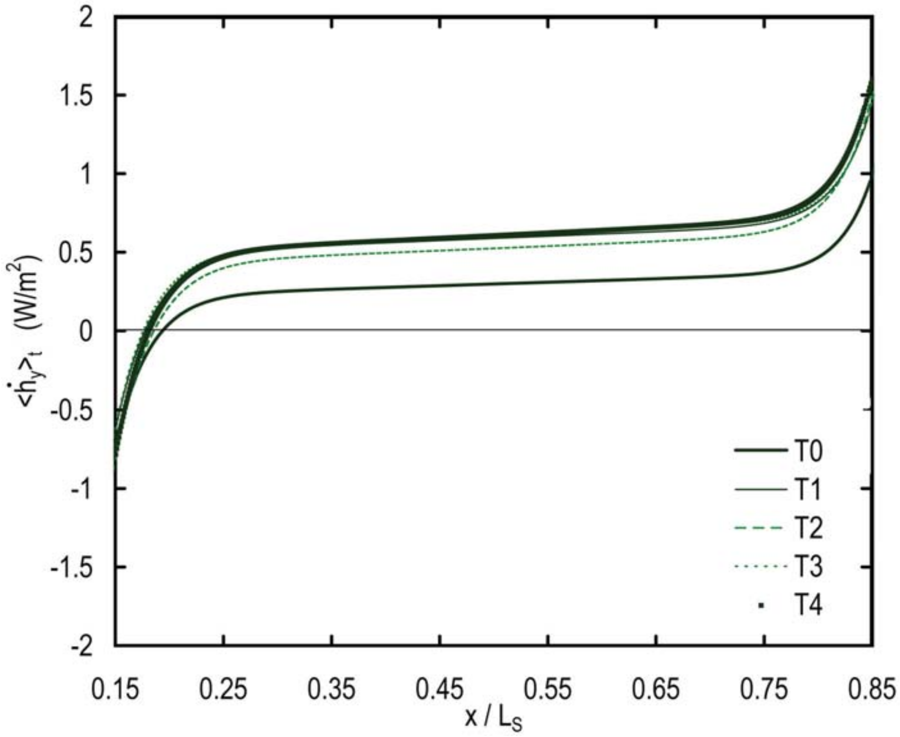

Figure B.11: Normalised stack position x/L_S versus time-averaged transverse heat flux $\left\langle \dot{h}_y \right\rangle_t$ for the stack midsection in Case A using selected timescale profiles.

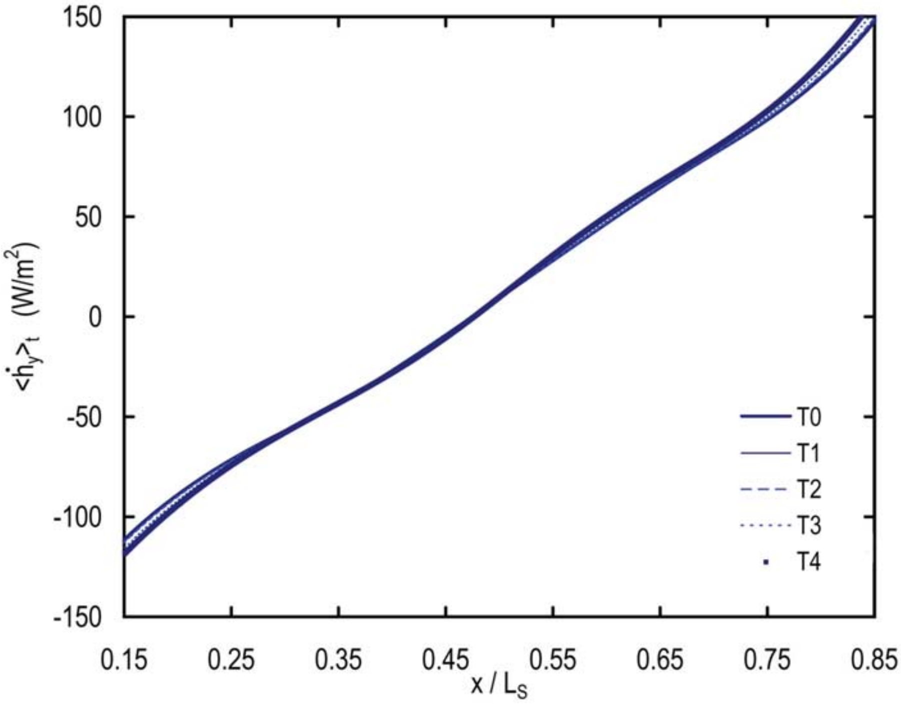

Figure B.12: Normalised stack position x/L_S versus time-averaged transverse heat flux $\left\langle \dot{h}_y \right\rangle_t$ for the stack midsection in Case B using selected timescale profiles.

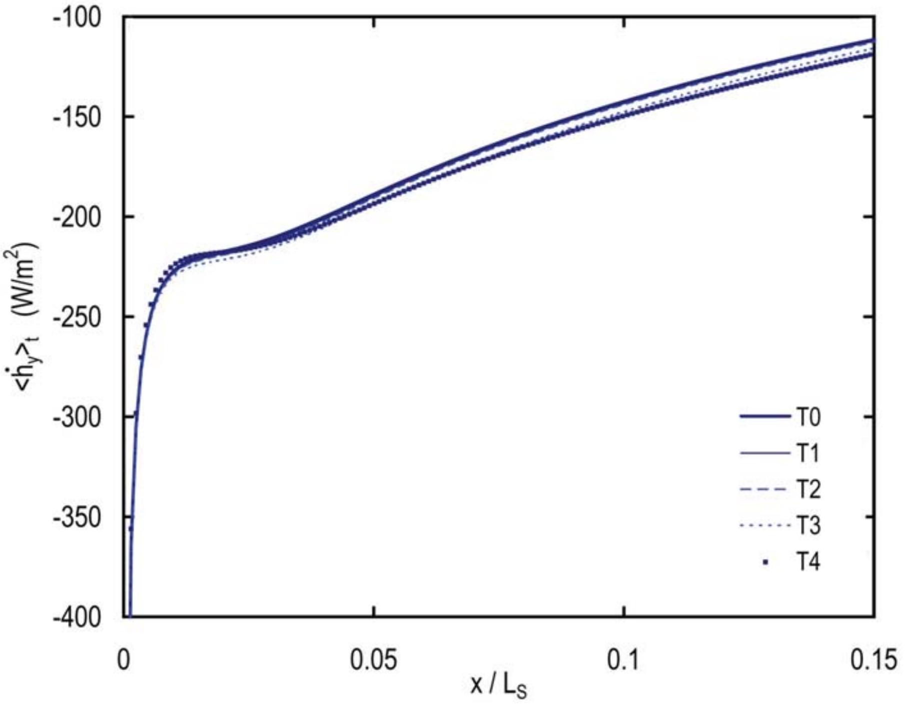

Figure B.13: Normalised stack position x/L_S versus time-averaged transverse heat flux $\left\langle \dot{h}_y \right\rangle_t$ for the stack 'cold end' in Case B using selected timescale profiles.

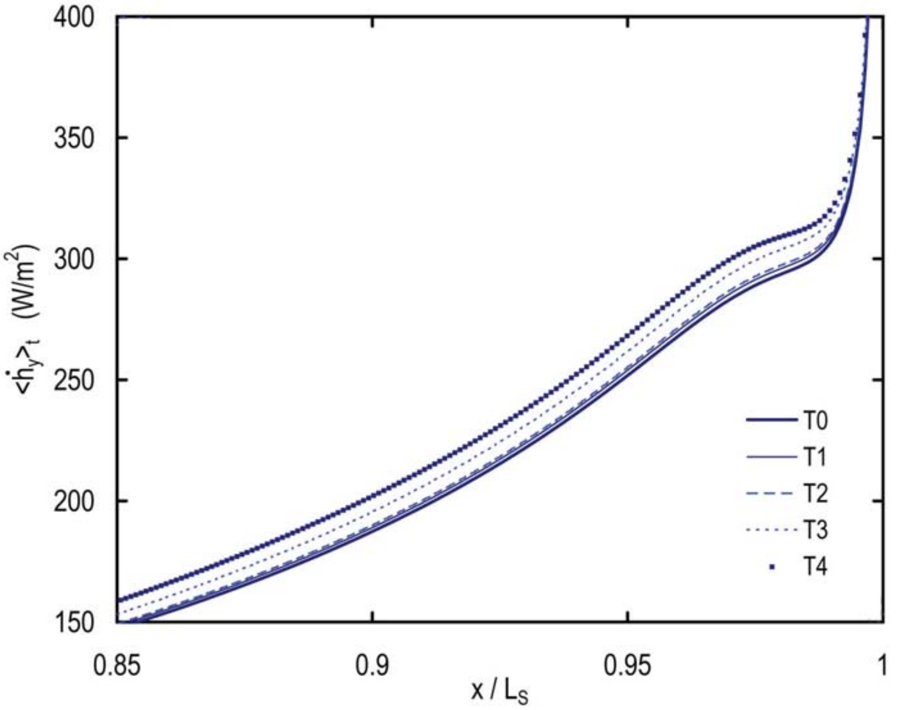

Figure B.14: Normalised stack position x/L_S versus time-averaged transverse heat flux $\left\langle \dot{h}_y \right\rangle_t$ for the stack 'hot end' in Case B using selected timescale profiles.

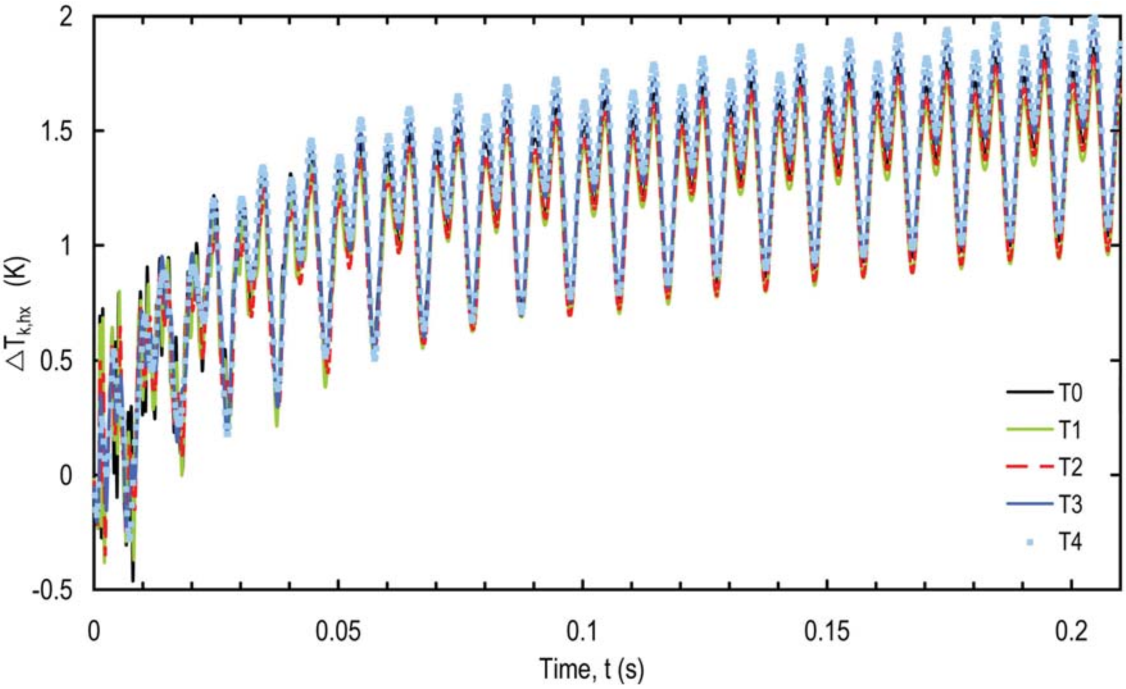

Figure B.15: $\Delta T_{k,hx}$ versus time for Case A with selected timescale profiles.

between 'T4' and the finer timescale profiles are more evident at the edges of the stack region, particularly at the 'hot' end. The coarser profiles appear to significantly overpredict $\left\langle \dot{h}_y \right\rangle_t$ at these locations.

The performance scale $\Delta T_{k,hx}$ (Equation (4.12), Section 4.1.5.1) defined in Section 4.1.5.1 is plotted in Figure B.15. It can be seen that for decreasing time step size, $\Delta T_{k,hx}$ is more unstable in the initial timeframe, and is expected to fluctuate within tighter limits at limit state (considered here to be 0.2s onwards).

Figure B.16 presents the values of $\Delta T_{k,hx}$ for both Case A and B over the time period 0.2s to 0.21s. Whilst it is presumable that a higher $\Delta T_{k,hx}$ is obtained in Case B from modelling a higher drive ratio, the greater variance in the $\Delta T_{k,hx}$ plot for Case B is attributed to secondary flow effects with frequencies higher than the operating frequency of 100Hz. It is interesting to note that for Case A, there does not appear to be a clear degradation in accuracy for $\Delta T_{k,hx}$ for increasing time step size. Coarser profiles ‘T4’ and ‘T1’ overstate and understate the ‘T0’ profile result respectively. In Case B, where the finite thickness of the plate is important, use of the smaller time step profiles ‘T0’ and ‘T1’ leads to lower values of $\Delta T_{k,hx}$. Profiles with larger time steps, ‘T3’ and ‘T4’, deviate significantly around 0.201s and 0.206s (phases immediately following velocity maxima). It is concluded from Figure B.16 that whilst time profiles ‘T3’ and ‘T4’ may be suitable for Case A, they will introduce additional errors (at phases of high velocity) when used for conditions similar to Case B.

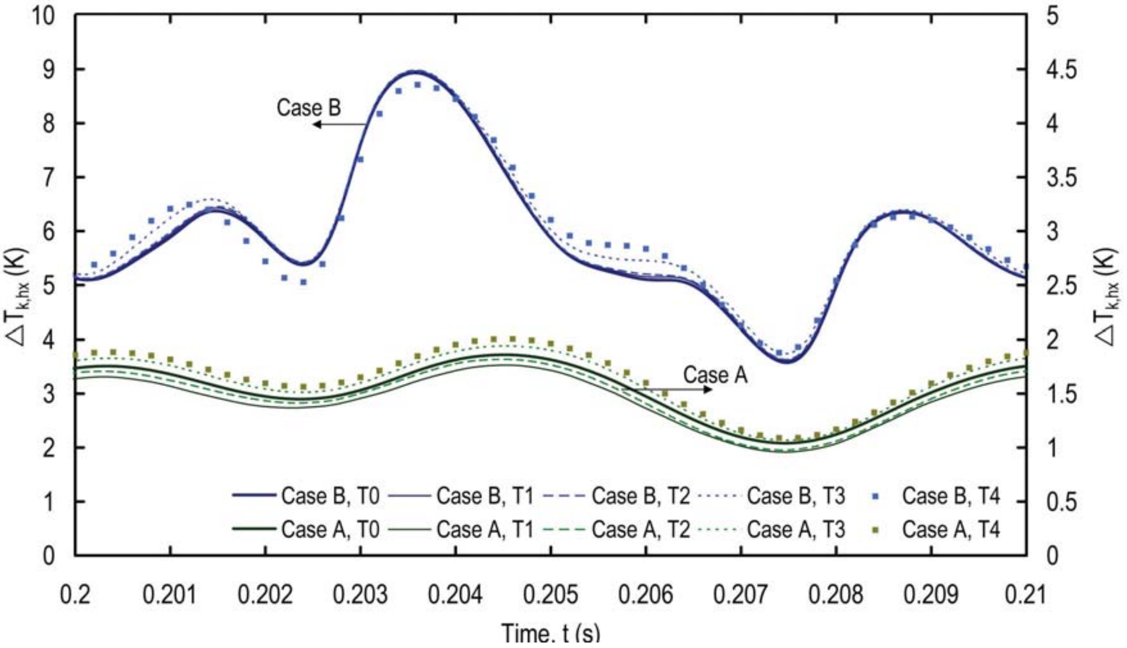

Figure B.16: $\Delta T_{k,hx}$ versus time for Cases A and B with selected timescale profiles.

Regardless, the coarser time profiles ‘T3’ and ‘T4’ should not be avoided on this basis alone, because time-averaging the $\Delta T_{k,hx}$ result presents a different perspective. The average value of $\Delta T_{k,hx}$ at each time step obtained over the time period 0.2s to 0.21s for each time step size is presented in Table B.8.

Using the finest time profile ‘T0’ as a basis, the errors of $\langle \Delta T_{k,hx} \rangle_t$ using time profiles ‘T2’ and ‘T3’ are less than that obtained using profile ‘T0’ for Case A.

Table B.8: $\langle \Delta T_{k,hx} \rangle_t$ (K) at limit state for various timestep sizes. Case files are otherwise identical to Runs 1 and 20 of Chapter 4. Using the finest time profile 'T0' as a basis, the comparative error in $\langle \Delta T_{k,hx} \rangle_t$ is also provided for each Case.

Case	T0 (0.1%)	T1 (0.2%)	T2 (0.5%)	T3 (1.0%)	T4 (2.0%)
A (Run 1, Chapt. 4)	1.5261	1.4318	1.4572	1.5902	1.6376
% Error (rel. T0)	-	6.2	3.3	4.2	7.3
B (Run 20, Chapt. 4)	5.9077	5.9449	5.9648	6.0573	6.0181
% Error (rel. T0)	-	0.63	0.96	2.5	1.9

Conversely, for Case B, time profiles 'T1' and 'T2' offer smaller errors than those time profiles with larger time step sizes. The increased computational cost of profiles 'T0' and 'T1' are considered excessive for the return in improved accuracy over 'T2', and as such 'T2' is selected for use in the studies presented in Chapters 5 and 6.

B.5 Temperature distributions over long numerical time scales

The study presented in this section is designed to provide comparison with the study of Kawamoto et al. (1998, Figure 10). Kawamoto et al. experimentally measured temperature distributions in thermoacoustic stacks without heat exchangers to investigate the potential error from 'steady streaming' when utilising conventional linear thermoacoustic formulations (Swift 1988). Of most interest to the current study are results presented for a stack comprising twenty 0.055mm-thick and 100mm-long sheets of Kapton spaced only $2y_0$=0.8mm apart and located in an acoustic standing-wave of $DR \approx$1.4% and $f \approx$535Hz. This study uses these operating conditions and a Rectangular edge profile as shown in Figure 5.1.

B.5.1 Modelspace

The apparatus used by Kawamoto et al. (1998) consisted of a circular tube of 0.426m length and 26mm internal diameter, closed at one end and excited at the other. The authors state that a pure standing-wave formed with 90° phasing between pressure and velocity. Using the system of modelling thermoacoustic couples presented in Section 3.1 and Appendices B and C, a computational domain L_{CV}=0.412m in length and y_0 tall was created. The right end of the domain represents a section of the closed end and the left end represents a cross section of the tube at which a pressure sensor was located in the actual unit. The entire device was stated to be oriented 'downwards' with the closed end at the bottom. Buoyancy effects were modelled by applying a gravitational force rightward (positive x direction) and equal to g=9.81m/s^2.

The stack plate was modelled as 100mm long with half-thickness t_s=0.0275mm. The stack plate was located 0.1m from the closed end of the tube and set to an initial temperature T_m. The solver profile 'S2' as defined in Section B.2, mesh profile 'G2' defined in Section B.3 and time profile 'T3' as defined in Section B.4 were used in acknowledging a need for reduced computational effort over solution precision when iterating an extremely large number of time steps.

Kawamoto et al. (1998) present the majority of their results in terms of the difference in temperature between the point of interest (axial position) and the cold side of the stack, $T_{k,c}$, and do not state the ambient temperature for each result obtained. Instead, the ambient gas speed of the working fluid, helium, is stated, and for this study T_m is therefore estimated using

$$T_m = \frac{c^2 M}{\gamma R} \tag{B.14}$$

to be approximately 313K, with molecular weight M=4.0026g/mol, γ=1.665, and R being the universal gas constant. The temperature distribution evaluated on y=0 and the performance metric $\Delta T_{k,hx}$ (Equation (5.3)) is used for comparison with experimental data.

B.5.2 Results

Figure B.17 presents the calculated time-averaged temperature distribution for comparison with the result of Kawamoto et al. (1998, Figure 10). The minimum time-averaged gas temperature $\langle T_k \rangle_{t,min}$ (obtained at the cold side of the stack) is subtracted from the time-averaged gas temperature distribution along y=0 (the line of symmetry between plates) and the result normalised by the maximum time-averaged gas temperature$\langle T_k \rangle_{t,max}$ is plotted versus axial position x. The shift in temperature distribution with increasing time suggests that the numerical model may approach a similar distribution to that experimentally determined by Kawamoto et al., which was sampled after the apparatus had operated for 20 minutes.

Figure B.18 presents the difference in temperature extremes on y=0 versus simulation time t. The experimental result of Kawamoto et al. (1998, Figure 10) obtained using similar operating conditions is ≈12K, which is exceeded in the computational result at t ≈1.2s. At t=4.2523s, or the 455,000th timestep, the difference in gas temperature is ≈31.4K and increasing, although curve-fitting techniques suggest that the rate of change of this value is decreasing with solution time. This discrepancy demonstrates that without accurate consideration of the external boundary conditions, energy states in the model are unlikely to converge to values representative of that obtained in practice, considered a 'true' limit cycle state.

Note that the experimental temperature distribution was obtained using 0.1mm thick thermocouples attached to a central plate, so it is difficult to assign the experimental data explicitly to the gas temperature and not consider the solid wall temperature. An additional source of error may be due to the thermocouple wire being almost twice the width of the plate thickness ($2y_0$=0.055mm) and therefore a significant impedance to gas circulation.

Numerical simulations of thermoacoustic couples carried out by Worlikar et al. (1998, pp313-314) found that the calculated temperature difference across the stack increased logarithmically. In ensuring that the temperature difference across the stack stabilised to within set tolerances, more than 200 acoustic cycles were computed. Figure B.17 includes results from Run 1 until t=8.8785s, a timeframe which is inclusive of the 950,000th time step, or 4,750th cycle.

The approach to modelling thermoacoustic couples presented in Chapter 3 is biased towards accurately modelling the heat transportation mechanisms between the couple and the fluid, and associated flow structures which influence this result. The model must have excellent spatial and temporal resolution at the expense of increased computational time. Figure B.17 shows that extension of the solution timeframe past the 200th cycle as did Worlikar & Knio (1996) will not necessarily obtain 'true' limit cycle states for these choices of materials and operating conditions. Therefore the computational cost in obtaining a 'true' limit cycle state is considered here to be excessive. Close monitoring of the time-averaged temperature difference and advancing the simulation time until it has fully stabilised to within set tolerances is considered here to be an effective technique to enable comparison with experimental data which is recorded over much larger timeframes. However, the selection of boundary conditions and stack geometry is crucial. Without considerable insight into the method, conditions and experimental error for which the data was obtained, numerically obtained temperature difference results such as Figure B.17 are without practical benefit.

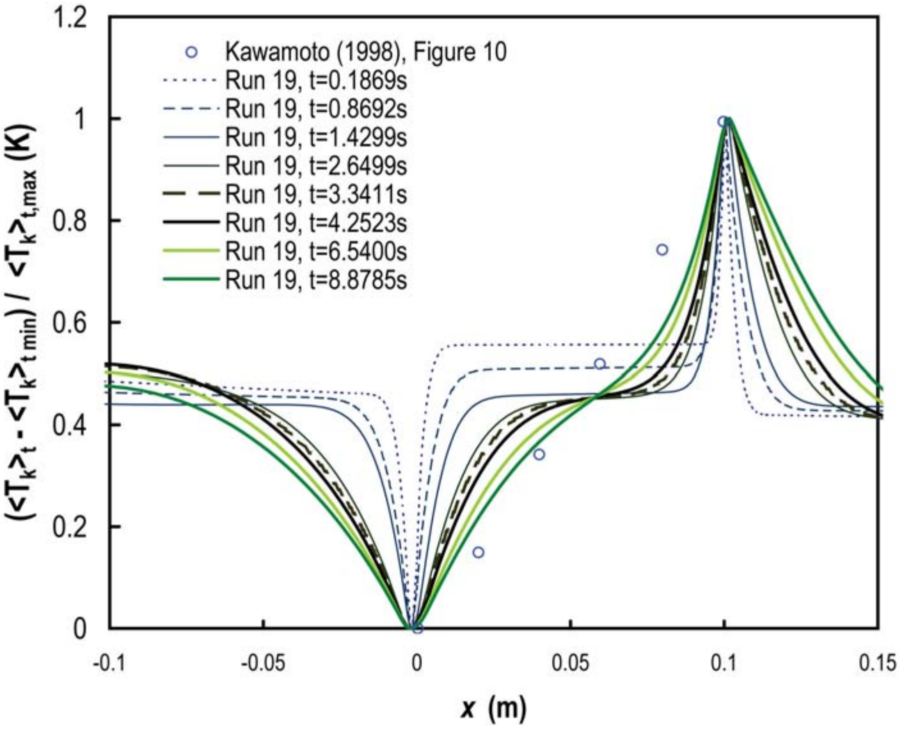

Figure B.17: Normalised difference in time-averaged gas temperature on y=0 versus axial position x for Run 19. The experimental result of Kawamoto et al. (1998, Figure 10) is provided for comparison.

Results indicate that if the calculations were to continue until the timescales were compatible with experimental results, similar proportions in the distribution of gas temperature are expected. That is, if the solution was advanced to $t \gg 5$ minutes, we could expect the time-averaged gas temperature distribution along y=0 to approach a straight line as demonstrated by Kawamoto et al. (1998).

Within the context of this thesis, the term ‘steady state’ is defined as the “state of operation or operating conditions in which the phase and magnitude of state variables such as p, U and T at each phase in the cycle do not vary from one oscillation to the next”. This is not the same as in an experimental sense, where the limit state may be observed from measured temperature differences obtained over timeframes three to four orders-of-magnitude larger.

Of course, if the simulation were to continue, it is expected that the rate

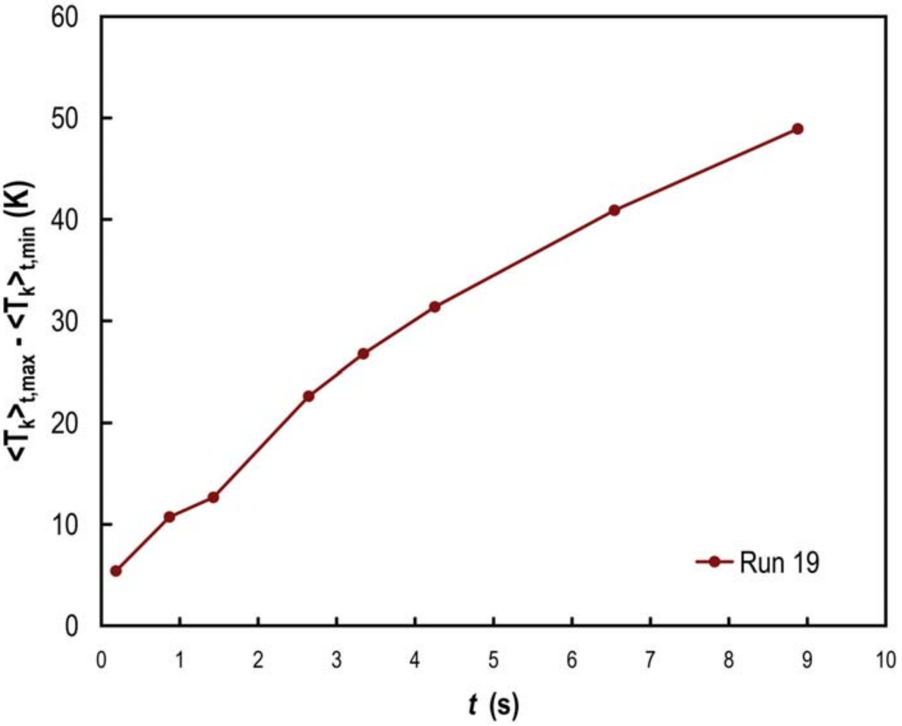

Figure B.18: Difference in temperature maxima and minima on y=0 versus simulation time t.

of system entropy, dS/dt, would approach zero. However, with dS/dt=0, the boundary conditions on the plate, end wall and inlet surfaces then control the rate of any energy transfer out of the domain, and any inaccuracies in imposed suitable boundary conditions may become so significant that comparisons with experimental data become difficult. This is particularly true for experimental results which report temperature measurements obtained after lengthy periods of time, i.e. in the order of minutes. This a key point of consideration when making direct comparisons between numerical predictions and experimental measurements, although it must also be remembered that advancing any existing numerical model of a thermoacoustic couple to the same physical timescales of experimental works is not yet computationally affordable. Such a model would still contain solution uncertainty from the set boundary conditions, assumptions regarding periodicity, and would only model two-dimensional flow.

The concerns raised in Section 3.2 regarding the applicability of the thermoacoustic couple numerical model to experimental studies are shown to be valid. Of two numerical models designed to enable comparison with quantitative and qualitative experimental data, results show good qualitative agreement in temperature and flow fields, but poor agreement in quantitative data. With reasonable estimates of the acoustic conditions and the construction geometry specific to the stack plates, flow fields are estimated using a single plate model which show good agreement. The accurate prediction of experimental measurements such as time-averaged temperature gradients within the solid structures requires intimate knowledge of the exterior geometry and/or thermal boundaries.

Appendix C

Post-processing techniques for use with distributed CFD computations

The bulk of the computational work presented in this thesis was completed on '*hydra*', an IBM eServer 1350 Linux cluster managed by the South Australian Partnership for Advanced Computing (SAPAC) at the University of Adelaide, and '*AC*', a SGI Altix 3700 Bx2 cluster at the Australian Partnership for Advanced Computing National Facility (APAC-NF). *hydra* has 128 nodes, each comprising one IBM xSeries 335 server with dual 2.4 GHz Intel Xeon processors (a multiprocessor-capable Pentium 4 architecture with 512 kilobytes of L2 cache memory) and 2 gigabytes of onboard RAM. *hydra* also has two terabytes of data storage. *AC* has 1,928 1.6Ghz Itanium2 processors with 256 kilobytes of L2 cache memory, but a much quicker interconnect between nodes (less than 2us MPI latency).

Although the commercial CFD code *Fluent* has a large capability for post-processing the results within the program environment, additional techniques were devised to extract data in forms comparable with previous studies and performance criteria specific to thermoacoustic devices.

On each cluster, a script file is used to input text commands to the *Fluent* environment on the host node in the parallel job. A sample of the script file submitted to the job handling system on *hydra* is shown as follows:

```
#!/bin/tcsh

#PBS -V
#PBS -q hydra
#PBS -N indy1_g4s3
#PBS -M luke.zoontjens@adelaide.edu.au
#PBS -m ae
#PBS -j oe
#PBS -l nodes=2:ppn=2,walltime=900:00:00

# Set number of processors, NP = "nodes" * "ppn"

set NP = 4


# dimensions flag options for fluent: 2d, 2ddp, 3d, 3ddp
set DIM = 2ddp

cd $PBS_O_WORKDIR
set PROG="/opt/shared/Fluent.Inc/bin/fluent"


# Use <set PROGARGS="$DIM -g"> for single CPU, other for parallel

# set PROGARGS="$DIM -g"
set PROGARGS="$DIM -g -t$NP -pnmpi -cnf=$PBS_NODEFILE"


set infile = $PBS_O_WORKDIR/input.txt

# Call the Fluent program, use commands $infile and write console to output.log

$PROG $PROGARGS < $infile >& $PBS_O_WORKDIR/output.log
```

where the file input.txt in the same file directory would contain a set of commands which depend on the post-processing technique used.

The following subsections discuss various methods used to obtain the results presented in Sections 4 to 6.

C.1 Time-averaged heat transfer rate

An important benchmark for the performance of a thermoacoustic couple, and therefore thermoacoustic stack, is the integral of $\left\langle \dot{h}_y \right\rangle_t$, the time-averaged rate of transverse heat flux through the material surface. The larger the value of $\left\langle \dot{h}_y \right\rangle_t$, the higher the performance of the thermoacoustic stack and hence system. As previous studies did not consider the physical thickness of the stack plates, the axial transverse heat flux $\left\langle \dot{h}_x \right\rangle_t$ via the edges of the stack was previously neglected or assumed negligible. For comparison with these studies, the method used to calculate $\left\langle \dot{h}_y \right\rangle_t$ is presented here, and obtaining $\left\langle \dot{h}_x \right\rangle_t$ can be achieved in similar fashion.

The input.txt file used to extract this data would include the following:

```
rcd indy1_g4s3 ........................./* read case and data */
solve/dual-time-iterate
2000 ................................../* 2,000 timesteps */
5000 ................................../* max. 5,000 iterations per timestep */
y
y
y
y ..................................../* overwrite existing monitor files */
solve/set/data-sampling ................/* turn on data statistic modes */
yes
solve/monitors/statistic/monitors ....../* enable statistics for monitor files */
yes
yes
solve/monitors/statistic/print ........./* print statistics for monitor files */
yes
plot/plot
no
hxhf2000.xy .........................../* filename for 2,000th timestep */
yes
no
no
heat-flux
yes
1
0
wall-shadow .........................../* heat exchanger surface name */
() ..................................../* resets console */
solve/dual-time-iterate ................/* iterate to 2,001st timestep */
1
5000
y
```

```
y
y
y
plot/plot
no
hxhf2001.xy .........................../* filename for 2,001st timestep */
yes
no
no
heat-flux
yes
1
0
wall-shadow
()
solve/dual-time-iterate .............../* iterate to 2,002nd timestep, etc. */
1
5000
...
```

The first line of input.txt instructs *Fluent* to read the case and data files of the model designated 'indy1_g4s3'. The next 3 lines instruct *Fluent* to solve the model over 2000 time-steps with a maximum of 5000 iterations per time step. Since, in this example, the directory the model is located in contains four surface monitor files (.out) files, the next 4 lines of 'y' will authorise *Fluent* to append new results to each file. With a correctly formulated and initialised model, this is sufficient instruction for *Fluent* to advance the model to limit-state operation.

Once the model has advanced to the 2,000th time step, the next 7 lines in input.txt instruct *Fluent* to perform the following in order: invoke data-sampling of unsteady flow statistics; monitor solver time statistics; and plot those time statistics to the console window. The remainder of the input.txt file now advances the model one time-step at a time, pausing to save the transverse heat flux distribution $\dot{h}_y$ across the plate surface ("wall-shadow") for each timeframe. The transverse heat flux distribution is saved into hxhf2000.xy, hxhf2001.xy, hxhf2002.xy, for the 2000th, 2001st, 2002nd time step and so forth. The script continues to advance the model until one full period of oscillation has been captured, and a .xy file describing the distribution of $\dot{h}_y$ for each time step in that period has been saved.

A *MATLAB* script file is used to automatically extract the data from each .xy file and collate the data into a matrix of size [number of grid points on surface "wall-shadow"] by [number of time steps]. The data within this matrix can now be displayed as a surface plot of $\dot{h}_y$ using the *MATLAB* **surf** command (Figure C.1).

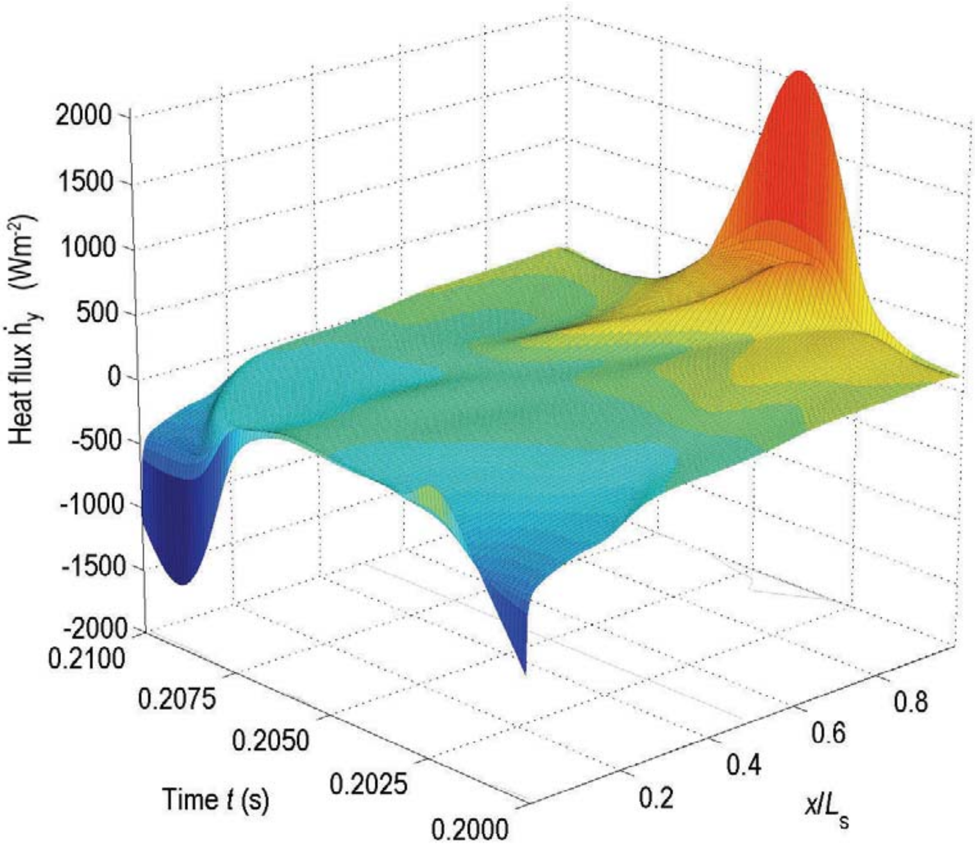

Figure C.1: Example of a surface contour plot showing the evolution of transverse heat flux $\dot{h}_y$ over the surface of a thermoacoustic couple. Data is shown for Run 20 of Chapter 4.

It can be seen from Figure C.1 that whilst the peak heat flux occurs at the plate extremities, there are subtle shifts in $\dot{h}_y$ within the stack region. These shifts are difficult to see if the mean heat flux across the plate due to bulk gas compression is also included in the figure. If an assumption is made that the temperature shift

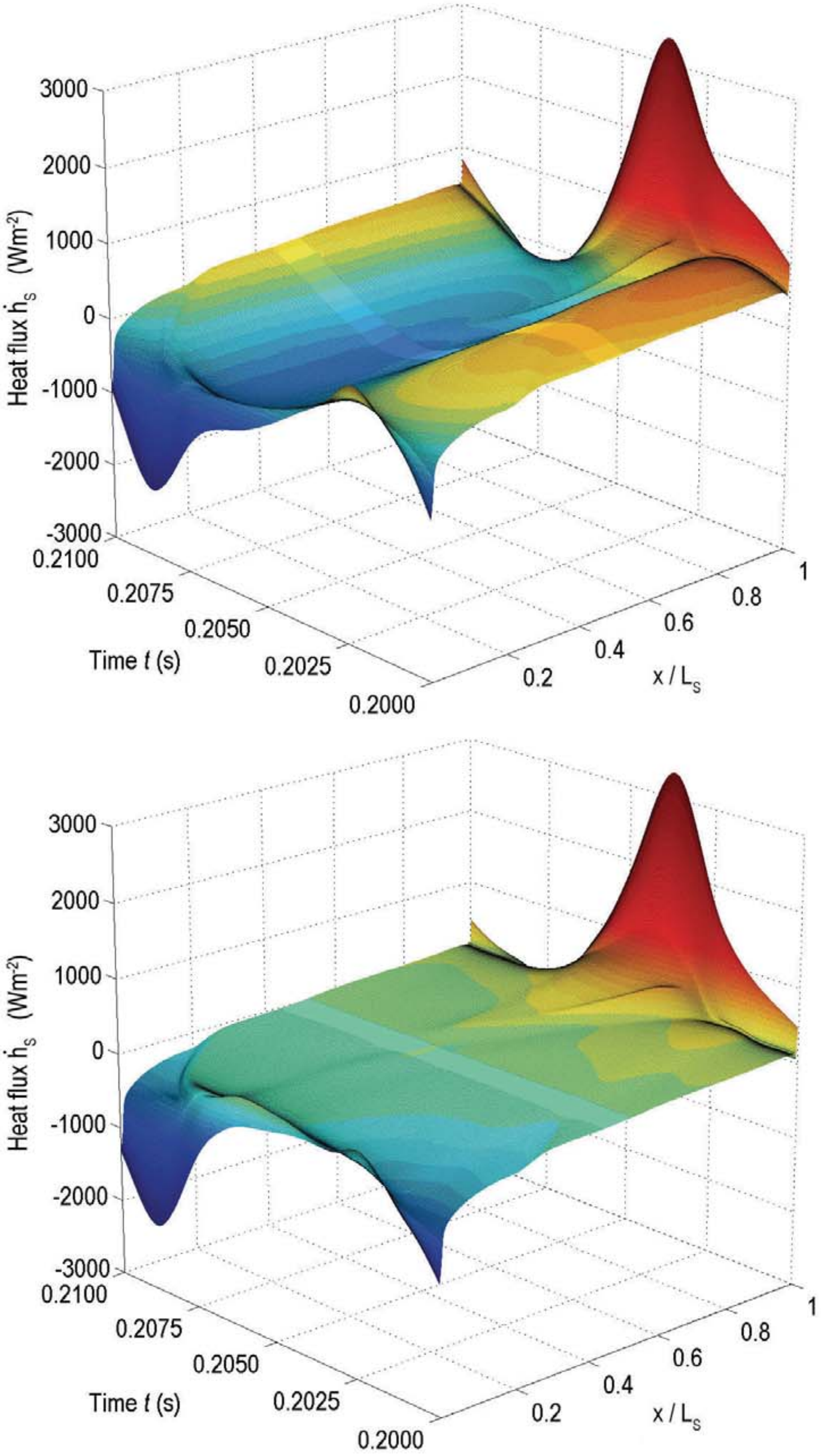

Figure C.2: Surface contour plot of $\dot{h}_S$ from Run 17 of Chapter 5, without (a) and with (b) removal of bulk gas compression effects.

across the plate is effectively uniform, then subtracting the value of $\dot{h}_y$ at the point where $\langle \dot{h}_y \rangle_t = 0$ removes the 'floating' flux value. The result is that effective heat transfer between the gas and solid is retained and is clearly presented. This effect is demonstrated in Figure C.2.

C.2 Temperature shifts

The performance measure $\Delta T_{k,hx}$ (Section 4.1.5.1) may be a useful measure of the performance of a thermoacoustic couple but is calculated based upon the temperature at the stack region extremities, i.e. x=0 and x=L_s (Figure 4.3(b)). Using a similar procedure to that described in Section C.1, the temperature along the mid-spacing of the stack region, that is y=0 (Figure 3.1), is surface plotted versus time and position. Figure C.3 presents an example of such a surface plot. It can be

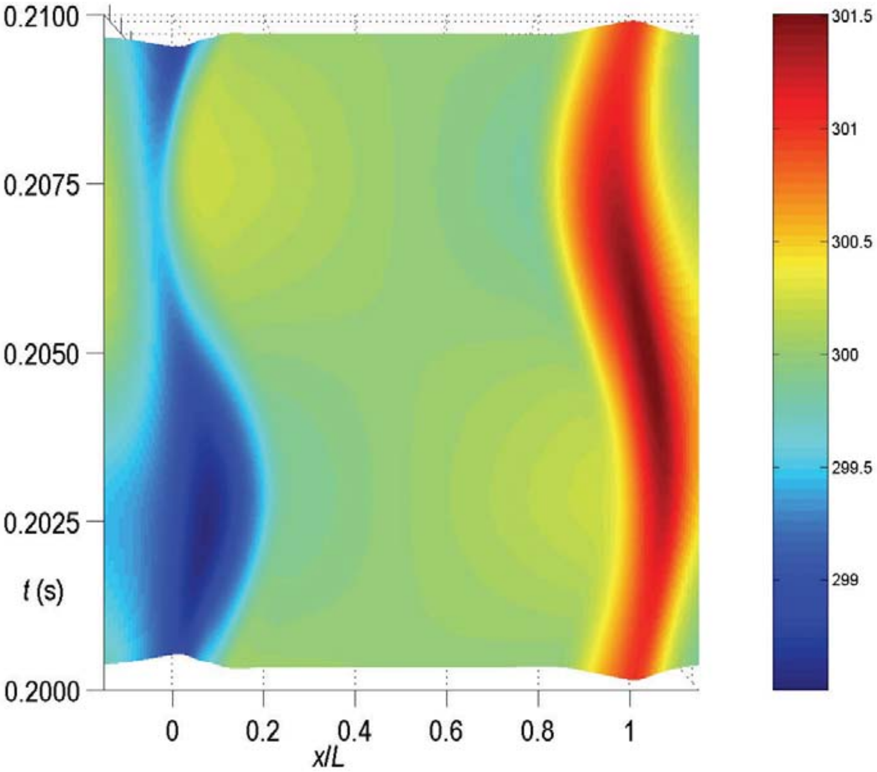

Figure C.3: Surface plot of temperature along y=0 for Run 5 of Chapter 5, t 0.2s to 0.21s. Plot is normalised by the temperature at (0,0.126m) to remove bulk gas compression effects.

clearly seen from this figure that the effective cold and hot zones in the vicinity of a thermoacoustic couple form at distance from the stack region, and move axially. Regardless, it is the author's opinion that $\Delta T_{k,hx}$ enables robust characterisation of the relative performance of a thermoacoustic couple.

C.3 Thermodynamic cycles

The thermodynamic cycles at set locations in the thermoacoustic couple are determined by simultaneous monitoring of pressure, entropy, temperature and other properties of interest for each point, then using a spreadsheet to plot relationships using the same time frames. Unfortunately, the output of each monitor is saved to an individual file in the form ⟨name⟩.out, and integrating each .out file in a collective spreadsheet is time-consuming.

The solution used was to develop a suitable notation system and post-processing methods to automatically build a spreadsheet which could then be manipulated to analyse the data and extract evident trends on a shorter timeframe. The notation system used was simply in the form

⟨location⟩_⟨property⟩.out.

For example, the monitor of pressure at location 'C2' (Table 4.3, Section 4) was **c2_p.out**.

All of the .out files for that run were then placed into a working directory and a script file implemented in the MATLAB environment was used to extract and collate the data, with columns ordered alphabetically and labelled using the filename of each .out file used. The output file could then be exported as a spreadsheet for quick post processing.

Temperature-entropy (‘T-s’) diagrams are useful in analysing compressible flows and can be used to discern whether fluid at certain locations act as ‘storage’ or ‘transfer’ elements, and are perturbed by the losses associated with flow disturbances or dissipative effects.

C.4 Visualisation of flow structures

The following sections detail the methods used to extract graphical information from each numerical study.

C.4.1 Velocity vector plots

Velocity vector diagrams show the instantaneous velocity of particles located at each cell in the domain and are colour coded and sized according to the velocity magnitude $|u|$. An example of a velocity vector plot is shown in Figure B.2. Because the flow is periodic, it is important to set a global scaling for velocity plots at different phases in the cycle, however it is difficult to know what scale to set without first running the model.

Velocity vector plots are obtained within *Fluent* by first running the model to limit state and then interrogating the model result file for u_{max}. The most time efficient method of extracting velocity vector plots throughout a limit-state cycle was to use the built-in Animation function within *Fluent*, in which vector plots for each time step are obtained in bitmap form and manipulated using a graphics editor.

C.4.2 Pathlines

Streamlines are powerful visualisation tools as they can show the perturbation of flow around solid objects. Here, two-dimensional streamlines are defined as lines drawn tangential to the velocity vectors throughout the flow field and satisfy (Mills 1999, Equation 4.1)

$$\frac{du}{u} = \frac{dv}{v} \tag{C.1}$$

where u and v are the x and y components of velocity respectively. Pathlines are defined as following streamlines generated at each time step for steady flows, however this definition is acceptable in this application of unsteady flow, since through use of a sufficiently fine time step, pathlines are in effect generated instantaneously.

The implementation of *Fluent* on *hydra* does not support graphics drivers so the display of plot windows was only possible on a local desktop machine. *hydra* was used to advance the model to limit-state operation, such that CPU time on the local machine was minimised. Pathlines were generated within the *Fluent* environment at selected fluid nodes along x=0 (the left end of the plate) and at distances of 5mm and 10mm in each direction from the y-axis. These images were then automatically processed using an image manipulation program and presented as a series of pathlines to show the shifts in flow structure 'frame-by-frame'. Frames 0.01s apart (10 time steps at 1% time scaling) was found to balance the subtle change between each image and the overall image size.

Appendix D

Case studies

This appendix presents several studies which investigate the applicability of the model developed in Chapter 3 to numerical and experimental results obtained over much larger spatial and temporal scales. These studies give confidence that the simulation techniques employed in this thesis are suitably accurate.

Appendix D.1 presents numerical results obtained using the higher-order model developed in Chapter 3 are compared to that predicted by the linear prediction software *DeltaE*, despite the assumption of larger timescales in *DeltaE*. Appendix D.2 shows qualitative comparisons of temperature fields calculated using the numerical model and experimental data presented by Wetzel & Herman (2000). The results of a study regarding the relative performance of materials popular for use in the construction of practical thermoacoustic devices are provided in Appendix D.3.

D.1 Comparison of *DeltaE* predictions to the numerical model predictions

The results obtained in Runs 4, 5, 6 of Chapter 6 and Run 5 of Section D.3 were compared with the linear prediction software *DeltaE* (Ward & Swift 2001). Figure D.1 presents a sketch of the arrangement of segments used to create the linear model.

The full length of the theoretical half-wavelength resonator is modelled, with the sections comprising the stack located to the right of centre. The modelling of effective thermoacoustic stacks in *DeltaE* requires hot and cold heat exchangers (segment type 'HX'). The stack segment type for a parallel plate configuration is 'STKSLAB'. To represent a series of parallel thermoacoustic couples, both HX segments and the STKSLAB segment are set to identical values of material type, plate-spacing y_0 and blockage ratio BR. Smooth walls were assumed for the internal walls of the device, such that laminar flow profiles within *DeltaE* were utilised. The length of each HX segment is set to 5mm to strike a balance between the length of effective transverse heat transfer found in Chapters 4 (that also corresponds with Piccolo & Pistone (2006, Runs 4 to 7)) and ensuring that the STKSLAB segment is primarily involved in the performance of the overall system. Featureless duct sections are implemented as 'DUCT' segments, and are all insulated, forcing any heat transfer to the exterior via the heat exchangers.

D.1.1 Method

Within the *DeltaE* environment, a plot loop was created to obtain operating states at discrete values of the pressure amplitude $|p_1|$. Since the *DeltaE* environment requires finite values for the cross-sectional area of the device, and the numerical model presented in Section 3.1 assumes stack periodicity with a unit depth, the acoustic input power $\dot{E}_2$ was normalised by the cross-sectional width of the channel, y_{CV}. The normalised acoustic power $\dot{E}_2$ and overall COP were thus calculated using both *DeltaE* and *Fluent* environments for comparison.

D.1.2 Results

Figure D.2 presents the estimated COP of a thermoacoustic couple determined using the linear prediction tool *DeltaE* and the numerical model. *DeltaE* is shown to give excellent agreement for a drive ratio of approximately 3.4%, but shows an

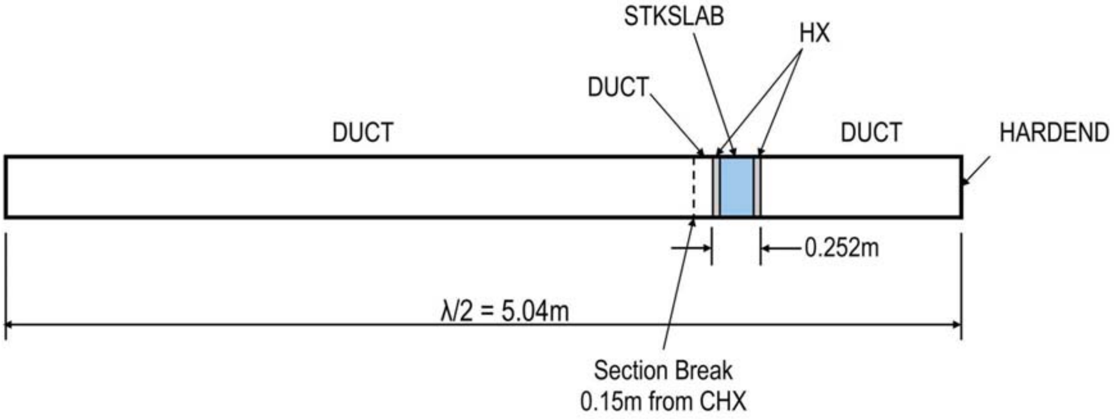

Figure D.1: Sketch of *DeltaE* segment arrangement and overall dimensions.

increasing trend in COP with drive ratio. This is expected since acoustic streaming or turbulence were not modelled in *DeltaE*.

Figure D.3 presents the normalised acoustic power per unit width $\dot{E}_2/y_0$ versus acoustic pressure amplitude as determined using the linear prediction tool *DeltaE* and the numerical model. Similar trends in $\dot{E}_2/y_0$ are predicted using the numerical and linear models.

In summary, the linear prediction tool *DeltaE* was used to predict the performance of the numerical model by simulating a half-wavelength resonator and using equivalent inputs for material properties and stack geometry. The linear prediction tool gave reasonably good estimates of the required acoustic energy flux to achieve a prescribed temperature difference across the stack achieved in the numerical model. *DeltaE* was also used to accurately predict the overall COP of the device for a drive ratio of approximately 3.4%, but provided less agreement at other drive ratios considered.

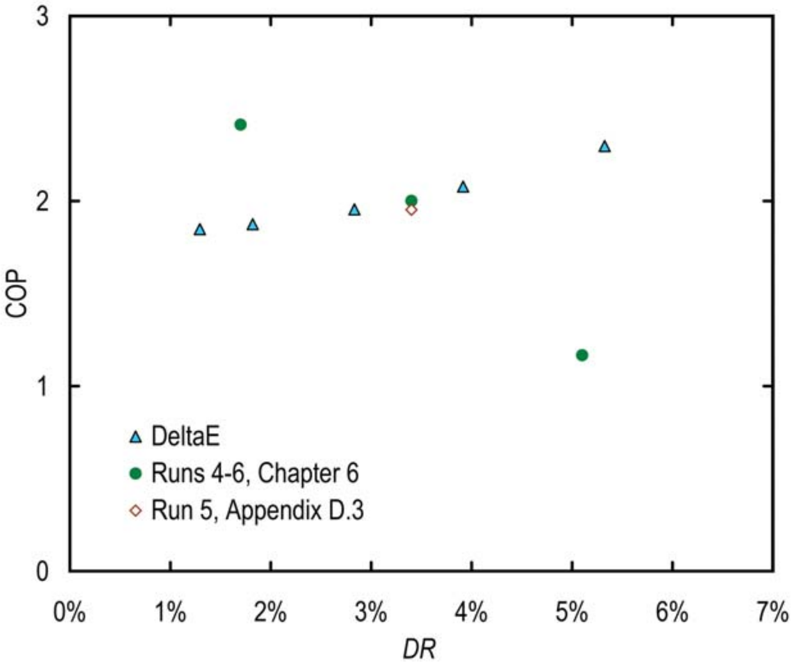

Figure D.2: COP versus drive ratio DR as calculated using the higher order model (Runs 4, 5, 6 of Chapter 6 and Run 5 of Section D.3) and the linear prediction tool *DeltaE*. p_m=1 bar.

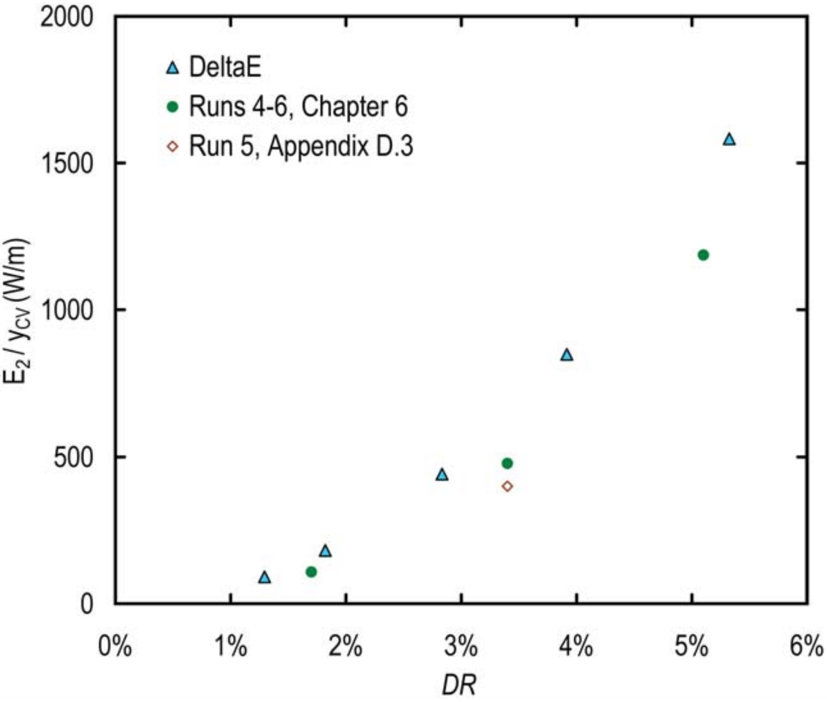

Figure D.3: $\dot{E}_2/y_0$ versus drive ratio DR as calculated using the higher order model (Runs 4, 5, 6 of Chapter 6 and Run 5 of Section D.3) and the linear prediction tool *DeltaE*.

D.2 Comparison of numerical predictions with experimental data

The research literature includes several publications of experimental results obtained from thermoacoustic devices which are without heat exchangers (stack only), use parallel-plate stacks and operate in a standing-wave mode. Such publications also report data in terms of steady-state temperature differentials. These results may be suitable for comparison with computational studies which use the thermoacoustic couple model described in Chapter 3 and Appendix B.

The conditions for which results are presented in Figure 6 of Wetzel & Herman (2000) are recreated in this study using the computational domain presented in Section 4.1.1.

Wetzel & Herman (1999, 2000) developed an experimental method for the measurement of time-averaged temperature fields in thermoacoustic devices and implemented it using an experimental device at atmospheric pressure. The thermoacoustic device was rectangular in cross section, and driven at one end using a loudspeaker. The measurement system was trained on the 'hot end' of a stack of two parallel plates 3mm in thickness with an applied temperature gradient. A series of resistive heating elements embedded into the midsection of each 3mm stack plate were used to generate a linear temperature gradient along the length of the plates, from approximately 75°C (Wetzel & Herman 2000, Figure 8, DR=1%) at the hot end to ambient temperature T_m (set to 294K) at the 'cold end'. The drive ratio was set to 1.7%.

D.2.1 Modelspace and operating conditions

The imposed temperature distribution was simulated in the *Fluent* environment by forcing the temperature of the stack plate T_s to be

$$T_s = T_m + \frac{dT}{dx}x \tag{D.1}$$

and independent of y. With L_s=0.076 the temperature gradient was therefore dT/dx=710.5K/m. It is unlikely that a smooth linear temperature distribution corresponding to Equation (D.1) was achieved in the experimental study using a finite number of heating elements, and experimental results published by Wetzel & Herman (2000, Figures 6 and 7) suggest that the plate edge at the hot end was slightly cooler than just inside the stack where the nearest heating element was located. Modifying the numerical model to include the conduction of heat from discrete heating elements may improve the correlation between boundary conditions in the numerical and experimental environments. However, the objective of the current study is to investigate whether the model presented in Section 3 is useful at predicting experimental data despite such limitations.

D.2.2 Results

The simulation results presented in this section enable comparison with the study of Wetzel & Herman (2000, Figure 3), which presented images of ‘quasi-isotherms’ or regions of gas at equal temperature. These images of quasi-isotherms were captured using ‘dry ice’ (subliminated carbon dioxide) as a visualisation medium. Contours of gas temperature T_k from selected time instants (calculated using the numerical model) are provided in Figure D.4 for comparison. It is difficult to ascertain which phases in the acoustic cycle correspond to the figures provided by Wetzel & Herman, however some qualitative similarities are apparent between the simulation results and the experimental results.

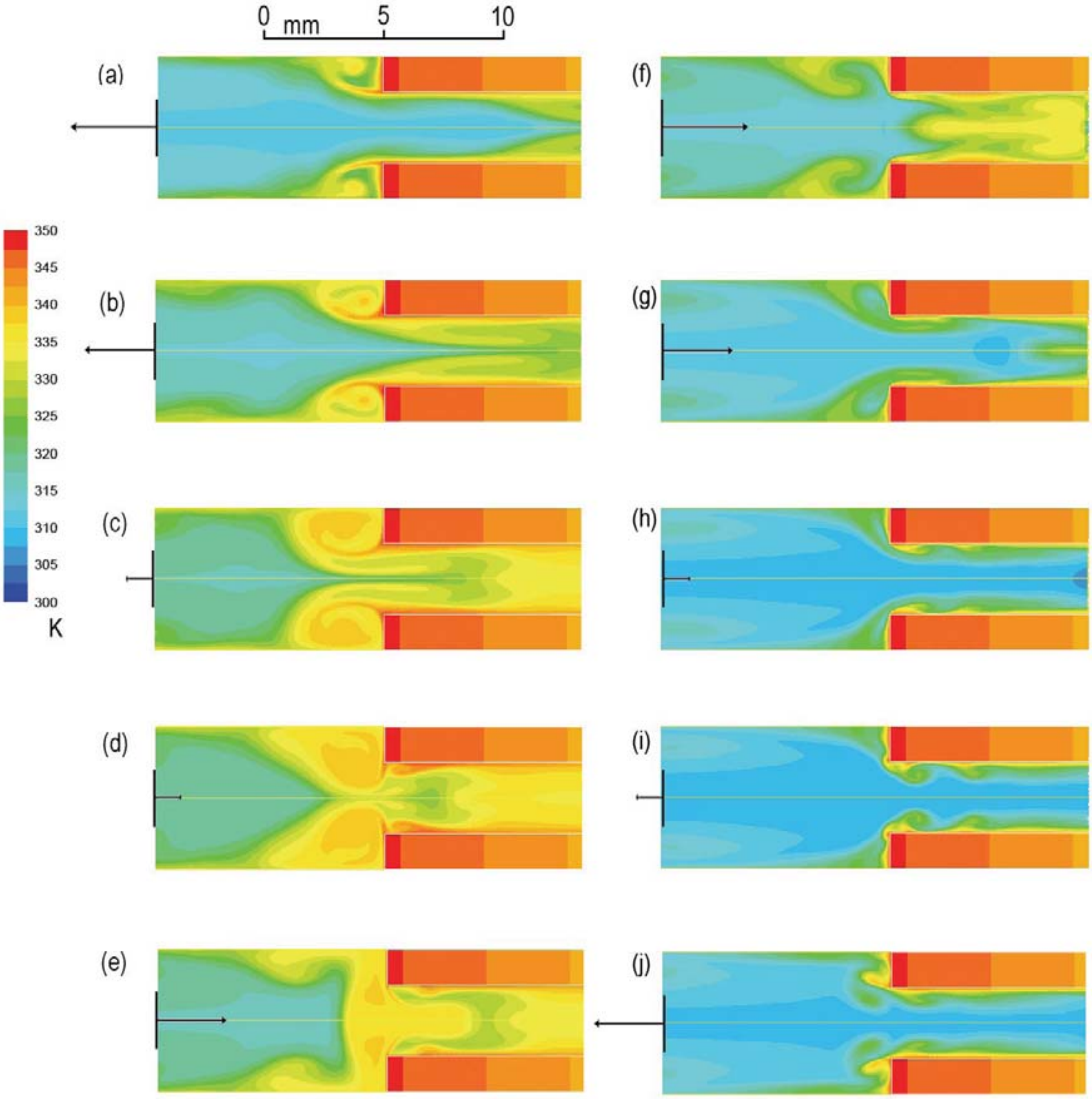

Figure D.4: Evolution of temperature contours over a complete oscillatory cycle (‘Hot’ end shown with image horizontally reversed and mirrored across y=0 for comparison with Wetzel & Herman (2000, Figure 3)). Phase is (a) ϕ=0°, (b) ϕ=36°, (c) ϕ=72°, (d) ϕ=108°, (e) ϕ=144°, (f) ϕ=180°, (g) ϕ=216°, (h) ϕ=252°, (i) ϕ=288°, and (j) ϕ=324°. Flow direction is indicated at the left of each figure.

Figure D.4 presents the evolution in temperature contours over a complete cycle using ten images obtained at 36° phase intervals. Figure D.5 presents pathlines which correlate to the same time instants shown in Figure D.4. Figures D.5(a) and (b) show that as the prevailing gas stream is slowing and accelerating to the right, vortices developing at the stack plate edges thicken, and heat in the outer rings of

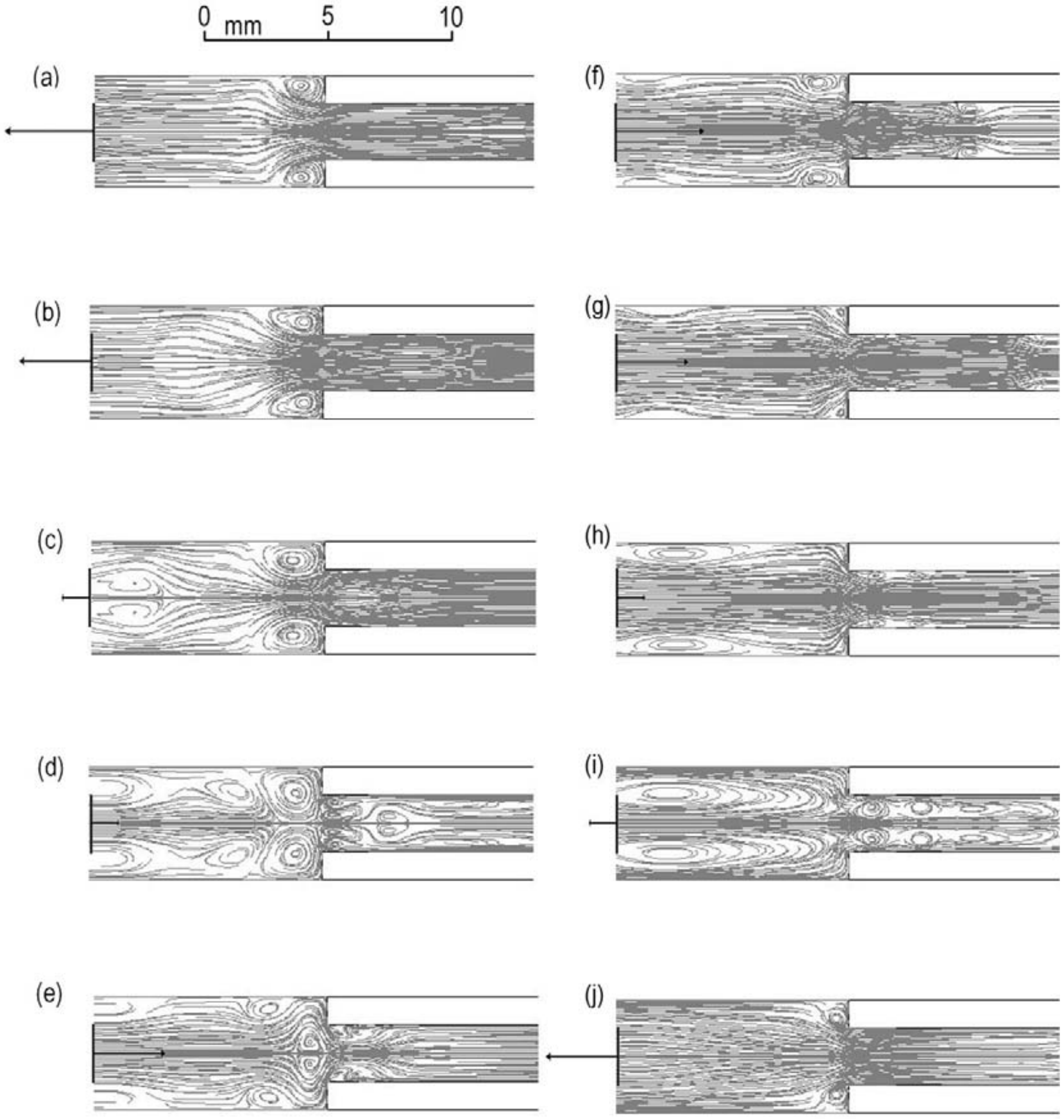

Figure D.5: Evolution of flow pathlines over a complete oscillatory cycle ('Hot' end shown with image horizontally reversed and mirrored across y=0 for comparison with Figure D.4). Phase is (a) ϕ=0°, (b) ϕ=36°, (c) ϕ=72°, (d) ϕ=108°, (e) ϕ=144°, (f) ϕ=180°, (g) ϕ=216°, (h) ϕ=252°, (i) ϕ=288°, and (j) ϕ=324°. Flow direction is indicated at the left of each figure.

each vortex diffuses into nearby stationary fluid (Figures D.5(c) and (d)). As shown in Sections 4.2.1 and 6.2.1, flow re-entering the stack region will enter at an oblique angle as a result of following the expanding vortex. Flow in Figures D.5(e) and (f) is now rightward and accelerating, however it is interesting to note that gas with residual heat forms trailing vortices outside the stack region which then impinge on the stack plate edge (Figure D.5(g)). The distribution in gas temperature at this

NOTE: This figure is included on page 235 of the print copy of the thesis held in the University of Adelaide Library.

Figure D.6: Visualisation of the flow field at the edges of the stack plates for the drive ratios (a) *DR*=1% and (b) *DR*=3%. (c) Schematic of the edge effects at the stack plates (Reproduced with permission (Wetzel & Herman 2000, Figure 3)). © Springer-Verlag 2000.

instant is qualitatively similar to the result presented by Wetzel & Herman (2000, Figure 3(c)).

Figures D.5(h) and D.5(i) show that as the rightward flow decelerates, the thermal boundary layer thickens. As the flow is accelerating leftward (as shown in Figure D.5(j)) the instabilities in the flow are 'ejected' by the leftward flow. A similar flow structure to Figure D.5(j) as well as Figures D.5(a) and D.5(b) can be seen in Figure 8 of the numerical study by Worlikar & Knio (1996), reproduced in Figure D.7.

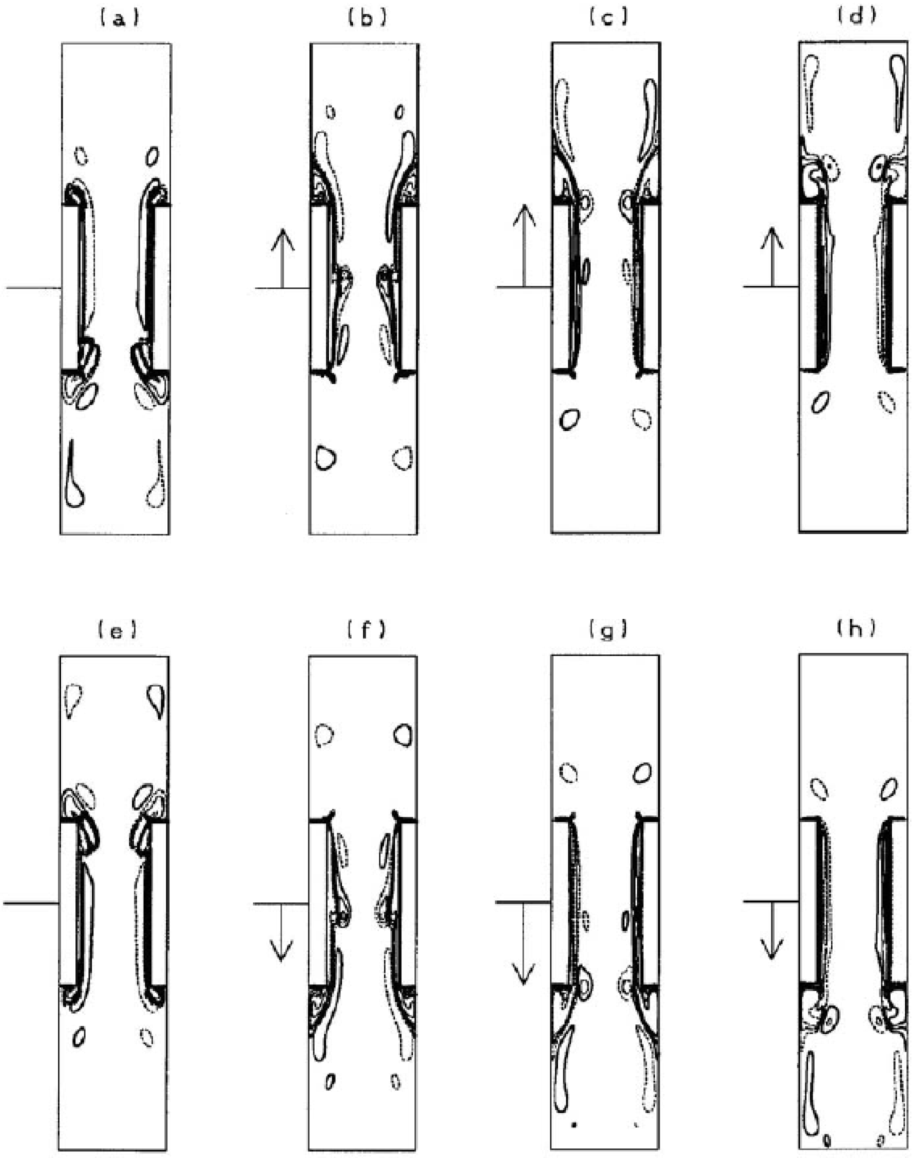

Figure D.7: Evolution of the vorticity field for case 6 of Worlikar & Knio (1996), using 45^{o} phase increments, i.e. (a) $t=32\pi/4$, (b) $t=33\pi/4$, (c) $t=34\pi/4$, (d) $t=35\pi/4$, (e) $t=36\pi/4$, (f) $t=37\pi/4$, (g) $t=38\pi/4$, and (h) $t=39\pi/4$ (Reproduced with permission (Worlikar & Knio 1996, Figure 8)). ©Elsevier Limited.

"Reprinted from *Journal of Computational Physics*, vol. 127 (2), Worlikar, A. S. & Knio, O. M., Numerical simulation of a thermoacoustic refrigerator. I. Unsteady adiabatic flow around the stack, pp. 424-451, Copyright (1996), with permission from Elsevier."

D.3 Performance comparisons of materials used in thermoacoustic couples

In this case study, materials popular for use in the construction of practical thermoacoustic devices are compared using identical flow conditions and stack geometry. This comparison may help determine which materials might be better suited for future investigation as thermoacoustic stack plates. A brief discussion of these materials and their implementation in the numerical model is presented in Section D.3.1.

The influence of thermophysical properties in the thermoacoustic couple model-space is evaluated within the scope of practical materials as discussed in Section D.3.1. Runs 1 to 6 are identical in terms of in operating conditions, working fluid and geometry, differing only in terms of stack material according to Table D.1. The computational domain for Runs 1 to 6 was adapted from Run 6 of Chapter 5, with DR set to 3.1% and p_m increased to 1 bar.

An aim of this study is to investigate whether the numerical model can be used to select materials for stack plates based upon desirable thermoacoustic performance characteristics, and hence performance metrics such as $\dot{Q}_{s,cold}$ and COP are used for comparison.

Table D.1: List of materials and operating conditions modelled in this case study. All runs model helium as the working fluid.

Run	Stack material	p_m (bar)	f (Hz)	$t_s/\delta_{\kappa m}$	$\lvert p_1\rvert/p_m$ (%)
1	Kapton	1.0	100	3.2	3.1
2	Mylar				
3	Stainless Steel				
4	Fibreglass				
5	Cordierite				
6	‘Ideal’				

D.3.1 Material models used in practical thermoacoustic couples

This subsection contains discussion of various materials specific to thermoacoustic device construction and their implementation in the computational environment. The working fluid modelled in this chapter is helium, using an ideal-gas law approximations for density and piecewise linear approximations of the thermal conductivity and dynamic viscosity. Thermophysical properties were taken from the published work of Mills (1999).

For the process of simulating thermoacoustic couples as described in Chapter 3, solid materials can be modelled on the basis of density ρ_s, heat capacity c_{ps} and heat conductivity k_s values only. Table D.2 contains a summary of the properties used for each of the materials discussed in the following subsections.

Table D.2: Comparison of thermophysical properties for modelling practical thermoacoustic devices.

Material	ρ_s kg/m^3	c_{ps} J/kgK	k_s W/mK	Service temp. (air) K
Kapton (Type HN)	1,420	1,080	0.120	4 - 670
Mylar	1,390	1,170	0.155	200 - 420
Stainless Steel (AISI Type 316)	8,238	468	13.0	200 - 1140
Fibreglass (NEMA G10)	1,800	1,670	0.288	220 - 410
Cordierite	2,510	1,460	2.60	≈240 - 1,370
'Ideal'	10^5	10^5	10^5	-

Celcor$^{\text{TM}}$ ceramic substrate properties Liu et al. (2006) showed that the porous construction of Celcor$^{\text{TM}}$type ceramic substrates led to discrepancies between the experimental and *DeltaE* results for system operating frequency and quality factor. Simulations using *DeltaE* to estimate the resonance frequency of their system were consistently 1% different from experimental tests. Liu et al. argued that increased thermal relaxation losses from transverse fluid flow within the porous ceramic walls was the mechanism by which this discrepancy occurs, since the linear model assumes impermeable stack walls. Using a polymerisation method they specifically developed for the task, the porosity of the stack was reduced, and their experimental results and *DeltaE* predictions agreed.

Ceramic substrates primarily comprise cordierite ($2MgO$-$2Al_2O_3$-$5SiO_2$), which is formed from a mixture of Kaolin or 'Kalil' ($2Al_2O_3$-$2SiO_2$-$2H_2O$), Talc

($3MgO$-$2Al_2O_3$-$4SiO_2$-$2H_2O$) and Alumina (Al_2O_3). The reported thermophysical properties of cordierite vary considerably depending on the fractions of each 'ingredient' and the manufacturing process efficiency. Corning Incorporated in New York, USA, a major manufacturer of ceramic substrates and the owner of the Celcor^{TM}, lists Celcor^{TM}cordierite with ρ_s=2,510kg/m^3, c_{ps} ≈1,110/kgK and k_s=1W/mK at 500°C (Technologies 2006). Hasselman et al. (1994) presented results for a cordierite matrix with density ρ_s=2,520kg/m^3, thermal capacity c_{ps}=798J/kgK and thermal conductivity k_s=4W/mK at room temperature.

For this study, values of density ρ_s=2,510kg/m^3, thermal capacity c_{ps}=1,460J/kgK and thermal conductivity k_s=2.6 W/mK are used based upon the majority of reported values for room temperature. Porosity was not modelled due to the significantly higher computational cost and considerations required to ensure numerical accuracy.

Polyimides Polymers of imide monomers or *polyimides* are in widespread use in the electronics industry (printed circuit boards, insulation) and also specialised applications such as aerospace life support and cryogenics. Polyimides are popular in thermoacoustics for their extremely low temperature range of operation and their availability in extremely thin sheets, which enables fabrication of very small stack and heat exchanger channels.

Polyimide films used in thermoacoustics are most likely *Kapton*^{TM}Type HN, with k_s ≈0.12W/mK, c_{ps} ≈1,080J/kgK and ρ_s ≈1,420kg/m^3 at 300K. Kapton film is available to the general consumer in thicknesses down to 25μm.

Polyesters Polyester films, like polyimides, are mass-produced for a wide range of industrial and commercial applications from plastic bottles to liquid crystal displays (LCDs). Biaxially-oriented polyethylene terephthalate is a polyester described as a thermoplastic film and is sold under the trade name *Mylar*$^{\mathrm{TM}}$. Mylar is useful in thermoacoustics primarily because of its stable mechanical stiffness over a wide range of temperatures, availability in sufficiently thin sections, low thermal conductivity and ease of handling. It is also regarded as environmentally friendly.

Mylar is often selected for the construction of stacks in experimental thermoacoustic heat-pumps and refrigerators (Poese & Garrett 2000, Tijani et al. 2002*a*, Herman & Travnicek 2006, Slaton & Zeegers 2006) and has also been considered in numerical studies of such devices (Ward & Swift 2001, Marx & Blanc-Benon 2005*a*). The properties of Mylar at 300K are taken as k_s=0.155W/mK, c_{ps}=1,170J/kgK and ρ_s=1,390kg/m^3 (*Product Information - Mylar - Physical-Thermal Properties* 2003) and to be available to the general consumer in thicknesses down to 12μm. With an upper service temperature limit of approximately 420K, mylar stacks are unsuitable for heat-engines or location near high temperature heat exchangers.

Fibreglass Fibreglass is useful for thermoacoustic applications due to its relatively low thermal conductivity, high flexural modulus to weight (rigidity for thin panels) and good thermal capacity. It is limited to use in thermoacoustic heat-pump applications since its maximum service temperature is around 410K.

In 1983 Wheatley et al. (1983) presented results for a demonstration thermoacoustic device which used fibreglass for stack plates. The fibreglass, which was a glass-epoxy laminate of grade 'NEMA G-10', is commonly used in electronics for printed circuit boards and is available in thin, rigid sheets. The thermal properties of G-10 fibreglass are taken as k_s=0.288W/mK, c_{ps}=1,670J/kgK and ρ_s=1,800kg/m^3.

Stainless Steel Stainless steel is a popular material used in thermoacoustics due to its favourable availability, service temperature range and mechanical properties. Stainless steel is commonly employed within thermoacoustic devices as a stack of mesh screens or a porous wool (Swift 2002, Section 8.2.2), however has also been used in the fabrication of parallel plate stacks (Backhaus & Swift 2001) and even pin array stacks (Hayden & Swift 1997).

To model AISI steel grade 316, a popular grade of stainless steel, the material properties k_s=13.0W/mK, c_{ps}=468J/kgK and ρ_s=8,238kg/m^3 are used.

D.3.2 Results and discussion

Figure D.8 presents the cooling power $\dot{Q}_{s,cold}$, input power $\dot{E}_2$, coefficient of performance COP and relative coefficient of performance COP_r obtained using Runs 1 to 5, each normalised by Run 6 (the 'Ideal' case). The results obtained from Runs 1 to 5 are shown to be within 4% of the result obtained using the 'Ideal' material modelled. The 'Ideal' material is set to approximate the 'ideal' material as defined within the *DeltaE* environment. Within *DeltaE*, the ideal material has infinite thermal capacity, density and conductivity, such that the influence of the stack material is negligible (Ward & Swift 2001, Appendix D). The results show that for the timescales and operating conditions simulated, there is little difference in the performance between the materials used in thermoacoustic couples.

The COP_r values obtained for stack plates manufactured of Fibreglass, Mylar and Kapton are shown to outperform the Ideal material and other material types simulated. This increase in efficiency is attributed to fact that these materials have comparably lower density and thermal conductivity, and hence lower thermal diffusivity.

In summary, the simulated performance of a variety of practical stack materials were compared for a thermoacoustic couple operating in helium at a drive ratio of 3.1%. Results were largely inconclusive due to the short timeframes and arbitrary

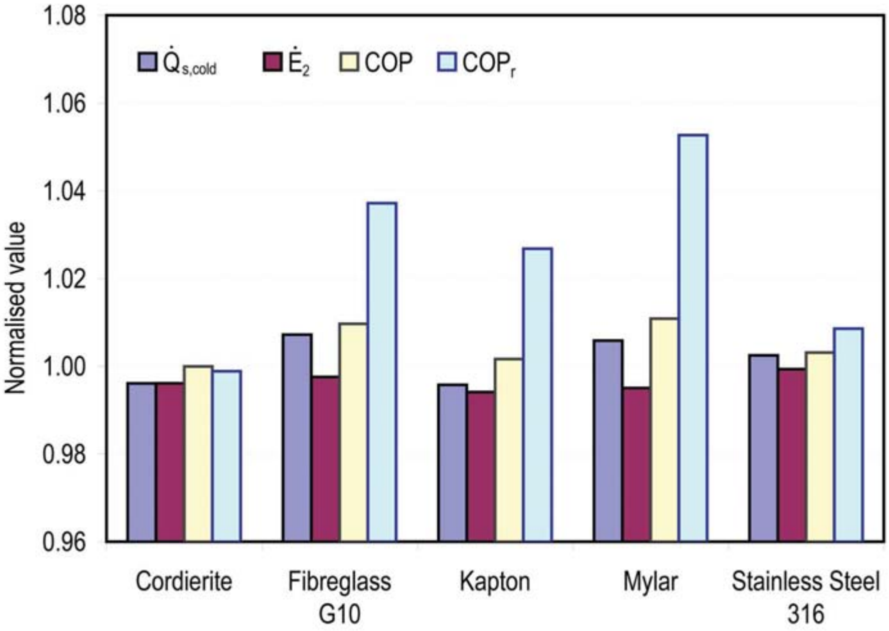

Figure D.8: Cooling power $\dot{Q}_{s,cold}$, $\dot{E}_2$, COP and COP_r for each material normalised by result obtained using Run 6.

boundary conditions associated with the system of modelling thermoacoustic couples used, however stack materials with lower thermal diffusivity were found to be more efficient on the basis of calculated COP_r.

Mylar is identified as the material of choice from the range of materials modelled, however for the reasons cited above this result is unqualified without wider investigation of the timescales involved and range of expected operating conditions.

Appendix E

Publications resulting from this thesis

Papers submitted to peer-reviewed journals from work resulting from this thesis are

- Zoontjens, L., Howard, C.Q., Zander, A.C. and Cazzolato, B.S. (2007) 'Numerical study of flow and energy fields in thermoacoustic couples of non-zero thickness', *International Journal of Thermal Sciences* (submitted) and
- Zoontjens, L., Howard, C.Q., Zander, A.C. and Cazzolato, B.S. (2007) 'Numerical comparison of thermoacoustic couples with modified stack plate edges', *International Journal of Heat and Mass Transfer* (submitted).
- Zoontjens, L., Howard, C.Q., Zander, A.C. and Cazzolato, B.S. (2006) 'Thermoacoustic air conditioners for the automotive industry', *Ecolibrium* (AIRAH) (submitted).
- Zoontjens, L., Howard, C.Q., Zander, A.C. and Cazzolato, B.S. (2006) 'Modelling and optimisation of acoustic inertance segments for thermoacoustic devices', *Proceedings of ACOUSTICS 2006*, 20-22 November 2006, Christchurch, New Zealand.

- Zoontjens, L., Howard, C.Q., Zander, A.C. and Cazzolato, B.S. (2005) 'Feasibility study of an automotive thermoacoustic refrigerator', *Proceedings of ACOUSTICS 2005*, 9-11 November 2005, Busselton, Western Australia.

References

Aktas, M. K. (2004), Thermoacoustically induced and acoustically driven flows and heat transfer in enclosures, PhD thesis, Department of Mechanical Engineering and Mechanics, Drexel University.

Aktas, M. K., Farouk, B., Narayan, P. & Wheatley, M. A. (2004), 'A numerical study of the generation and propagation of thermoacoustic waves in water', *Physics of Fluids* **16**(10), 3786–3794.

Allison, C. B. (2006), The effects of turbulence structures on the air-side performance of compact tube-fin heat exchangers, PhD thesis, School of Mechanical Engineering, The University of Adelaide, Australia.

Arnott, W. P., Bass, H. E. & Raspet, R. (1991), 'General formulation of thermoacoustics for stacks having arbitrarily shaped pore cross sections', *J. Acous. Soc. Am.* **90**(6), 3228–3237.

Atchley, A. A., Hofler, T. J., Muzzerall, M. L., Kite, M. D. & Ao, C. (1990), 'Acoustically generated temperature gradients in short plates', *J. Acous. Soc. Am.* **88**(1), 251–263.

Backhaus, S. & Swift, G. W. (2000), 'A thermoacoustic-Stirling heat engine: Detailed study', *J. Acoust. Soc. Am.* **107**(6), 3148–3166.

Backhaus, S. & Swift, G. W. (2001), Fabrication and use of parallel plate regenerators in thermoacoustic engines, *in* 'Proceedings from the 36th Intersociety Energy Conversion Engineering Conference (IECEC)', Vol. 1, pp. 1393–1398.

Backhaus, S. & Swift, G. W. (2002), 'New varieties of thermoacoustic engines', *Proceedings of the Ninth International Congress on Sound and Vibration, Orlando FL, USA, July 8-11* **Paper 502**.

Backhaus, S., Tward, E. & Petach, M. (2004), 'Traveling-wave thermoacoustic electric generator', *Applied Physics Letters* **85**(6), 1085–1087.

Bailliet, H., Gusev, V., Raspet, R. & Hiller, R. A. (2001), 'Acoustic streaming in closed thermoacoustic devices', *J. Acous. Soc. Am.* **110**(4), 1808–1821.

Bauwens, L. (1998), 'Thermoacoustics: Transient regimes and singular temperature profiles', *Physics of Fluids* **10**(4), 807–818.

Berson, A. & Blanc-Benon, P. (2007), ‘Nonperiodicity of the flow within the gap of a thermoacoustic couple at high amplitudes’, *J. Acoust. Soc. Am.* **122**(4), EL122–EL127.

Besnoin, E. (2001), Numerical study of thermoacoustic heat exchangers, PhD thesis, The Johns Hopkins University, Baltimore, Maryland, USA.

Blanc-Benon, P., Besnoin, E. & Knio, O. (2003), ‘Experimental and computational visualization of the flow field in a thermoacoustic stack’, *C. R. Mecanique* **331**, 17–24.

Boris, J., Landsberg, A. M., Oran, E. S. & Gardner, J. H. (1993), LCPFCT - a flux-corrected transport algorithm for solving generalized continuity equations, Technical Report 6410-93-7192, Laboratory for Computational Physics and Fluid Dynamics, Naval Research Laboratory, Washington, DC, USA.

Brown, M. A. & Churchill, S. W. (1999), ‘Finite-difference computation of the wave motion generated in a gas by a rapid increase in the bounding temperature’, *Computers and Chemical Engineering* **23**, 357–376.

Cao, N., Olsen, J. R., Swift, G. W. & Chen, S. (1996), ‘Energy flux density in a thermoacoustic couple’, *J. Acous. Soc. Am* **99**(6), 3456–3464.

Ceperley, P. H. (1979), ‘A pistonless Stirling engine - the traveling wave heat engine’, *J. Acoust. Soc. Am.* **66**(5), 1508–1513.

Chen, G. B. & Jin, T. (1999), ‘Experimental investigation on the onset and damping behaviour of the oscillation in a thermoacoustic prime mover’, *Cryogenics* **39**, 843–846.

Cook, R. R. (1999), *Assessment of uncertainties of measurement for calibration and testing laboratories*, National Association of Testing Authorities, Australia. ISBN 0-909307-46-6.

Courant, R., Friedrichs, K. & Lewy, H. (1928), ‘ber die partiellen differenzengleichungen der mathematischen physik’, *Mathematische Annalen* **100**(1), 32–74.

Curtis, S. B. (2000), Modification and verification of design simulation for thermoacoustic research software, Master’s thesis, Naval Postgraduate School, Monterey CA., USA.

Duffourd, S. (2001), Refrigerateur thermoacoustique: etudes analytiques et experimentales en vue d’une miniaturisation, PhD thesis, Ecole Centrale de Lyon, France.

Fares, E. & Schroder, W. (2004), ‘A general one-equation turbulence model for free shear and wall-bounded flows’, *Flow, Turbulence and Combustion* **73**, 187–215.

Farouk, B., Oran, E. S. & Fusegi, T. (2000), ‘Numerical study of thermoacoustic waves in an enclosure’, *Physics of Fluids* **12**(5), 1052–1061.

Feldman, K. T. (1966), A study of heat generated pressure oscillations in a closed end pipe, PhD thesis, Dept Mechanical Engineering, University of Missouri, USA.

FLUENT 6.2.16 User Manual (2006), Technical report, Fluent Inc.

Galiullina, E. R. & Botteldooren, D. (2006), Numerical simulation of streaming in resonator based thermoacoustic devices, *in* 'The Thirteenth International Congress on Sound and Vibration (ICSV13), Vienna, Austria'.

Galiullina, E. R., van Rentergam, T. & Botteldooren, D. (2005), 3D numerical model of secondary streaming in an acoustic-resonance tube refrigerator, *in* 'The Twelth International Congress on Sound and Vibration (ICSV13), Lisbon, Portugal'. Paper 474.

Gardner, D. L. & Swift, G. W. (2003), 'A cascade thermoacoustic engine', *J. Acoust. Soc. Am.* **114**(4), 1905–1919.

Garrett, S. L. (1997), 'High-power thermoacoustic refrigerator', US Patent No. 5647216.

Garrett, S. L. (2004), 'Resource letter: TA-1: Thermoacoustic engines and refrigerators', *Am. J. Phys.* **72**(1), 11–17.

Garrett, S. L. & Backhaus, S. (2000), 'The power of sound', *American Scientist* **88**(6), 516–525.

Gedeon, D. (1995), Sage: Object-oriented software for cryocooler design, *in* J. R.G. Ross, ed., 'Cryocoolers 8', pp. 281–292.

Gedeon, D. (1997), DC gas flows in stirling and pulse tube cryocoolers, *in* 'Proceedings of the 9th International Cryocooler Conference, edited by R.G. Ross', Plenum, New York, pp. 385–392.

Hamilton, M. F., Ilinskii, Y. A. & Zabolotskaya, E. A. (2003), 'Acoustic streaming generated by standing waves in two-dimensional channels of arbitrary width', *J. Acoust. Soc. Am.* **113**(1), 153–160.

Hantschk, C. & Vortmeyer, D. (2000), 'Numerical simulation of unsteady interactions between flow, heat conduction and acoustics within a Rijke tube', *Chemical Engineering and Technology* **23**(9), 758–763.

Hasselman, D. P. H., Donaldson, K. Y., Liu, J., Gauckler, L. J. & Ownby, P. D. (1994), 'Thermal conductivity of a particulate-diamond-reinforced cordierite matrix composite', *J. Am. Ceram. Soc.* **77**(7), 1757–1760.

Hatazawa, M., Sugita, H., Ogawa, T. & Seo, Y. (2004), 'Performance of a thermoacoustic sound wave generator driven with waste heat of automobile gasoline engine', *Transactions of the Japan Society of Mechanical Engineers (Part B)* **70**(689), 292–299.

Hayden, M. E. & Swift, G. W. (1997), 'Thermoacoustic relaxation in a pin-array stack', *J. Acous. Soc. Am.* **102**(5), 2714–2722.

Herman, C. & Travnicek, Z. (2006), 'Cool sound: the future of refrigeration? thermodynamic and heat transfer issues in thermoacoustic refrigeration', *Heat Mass Transfer* **42**, 492–500.

Higgins, B. (1802), *Journal of Natural Philosophy and Chemistry and Arts (Nicholson's Journal)* **I**(130).

Hofler, T. J. (1986), Thermoacoustic refrigerator design and performance, PhD thesis, Physics Department, University of California, San Diego, CA, USA.

Hofler, T. J. & Adeff, J. A. (2001), 'An optimized miniature Hofler tube', *Acoustics Research Letters Online* **2**(1), 37–42.

Ibrahim, M. B., R. C. Tew, J., Zhang, Z., Gedeon, D. & Simon, T. W. (2001), CFD modeling of free-piston Stirling engines, Technical Report TM-2001-211132, NASA Technical Memorandum.

Ishikawa, H. (1999), Investigations of optimum design of heat exchangers of thermoacoustic engines, PhD thesis, Department of Mechanical Engineering, The University of Queensland, Australia.

Ishikawa, H. (2001), Investigations of optimum design of heat exchangers of thermoacoustic engines, PhD thesis, Department of Mechanical Engineering, the University of Queensland, Australia.

Ishikawa, H. & Mee, D. J. (2002), 'Numerical investigations of flow and energy fields near a thermoacoustic couple', *J. Acous. Soc. Am.* **111**(2), 831–839.

Jin, T., Wang, B. & Zhang, S. (2003), 'Analysis of energy flow in regenerator of thermoacoustic engines', *Review of Scientific Instruments* **74**(1), 674–676.

Kawamoto, A., Ozawa, M. & Arikawa, F. (1998), 'Temperature distribution along stack in an acoustic-resonance tube: discussions on advanced linearized theory', *Heat Transfer - Japanese Research* **27**(8), 551–567.

Kornhauser, A. A. & Smith, Jr, J. L. (1989), Heat transfer with oscillating pressure and oscillating flow, *in* 'Proceedings of the Intersociety Energy Conversion Engineering Conference', Vol. 5, pp. 2347–2353.

Kotsubo, V. (2005), 'Sage and DeltaE for thermoacoustic modeling (a)', *J. Acous. Soc. Am.* **118**(3), 1926.

Liang, W. & de Waele, A. T. A. M. (2007), 'A new type of streaming in pulse tubes', *Cryogenics* . Article in press doi:10.1016/j.cryogenics.2007.04.

Liu, J., Garrett, L., Long, G. S. & Sen, A. (2006), 'Separation of thermoviscous losses in celcor$^{\mathrm{TM}}$ceramic', *J. Acous. Soc. Am.* **119**(2), 857–862.

Lycklama à Nijeholt, J. A., Tijani, M. E. H. & Spoelstra, S. (2005), 'Simulation of a travelling wave thermoacoustic engine using computational fluid dynamics', *J. Acous. Soc. Am.* **118**(4), 2265–2270.

Mahmud, S. & Fraser, R. A. (2005), 'Flow, thermal, and entropy generation characteristics inside a porous channel with viscous dissipation', *International Journal of Thermal Sciences* **44**, 21–32.

Marx, D. & Blanc-Benon, P. (2004*a*), 'Computation of the mean velocity field above a stack plate in a thermoacoustic refrigerator', *C.R. Mecanique* **332**, 867–874.

Marx, D. & Blanc-Benon, P. (2004*b*), 'Numerical simulation of stack-heat exchangers coupling in a thermoacoustic refrigerator', *AIAA Journal* **42**(7), 1338–1347.

Marx, D. & Blanc-Benon, P. (2005*a*), 'Numerical calculation of the temperature difference between the extremities of a thermoacoustic stack plate', *Cryogenics* **45**(3), 163–172.

Marx, D. & Blanc-Benon, P. (2005*b*), 'Computation of the temperature distortion in the stack of a standing wave thermoacoustic refrigerator', *J. Acous. Soc. Am.* **118**(5), 2993–2999.

Matveev, K. I. (2003), 'Energy consideration of the non-linear effects in a Rijke tube', *Journal of Fluids and Structures* **18**, 783–794.

Matveev, K. I. & Culick, F. E. C. (2003), 'A study of the transition to instability in a Rijke tube with axial temperature gradient', *J. Sound and Vibration* **264**, 689–706.

Merkli, P. & Thomann, H. (1975*a*), 'Transition to turbulence in oscillating pipe flow', *J. Fluid Mech.* **68**(3), 567–575.

Merkli, P. & Thomann, H. (1975*b*), 'Thermoacoustic effects in a resonance tube', *J. Fluid Mech.* **70**(1), 161–177.

Mills, A. F. (1999), *Heat Transfer*, 2nd edn, Prentice Hall, NJ, USA.

Mohd-Ghazali, N. & McHugh, J. P. (2003), Nonlinear simulation of acoustic waves in thermoacoustic resonator, *in* 'Computational Methods in Experimental Measurements XI', Vol. 4 of *Computational Engineering*, pp. 371–380. ISSN 1466-7266.

Mongeau, L., Alexander, A., Minner, B., Paek, I. & Braun, J. E. (2001), 'Experimental investigations of an electro-dynamically driven thermoacoustic cooler', *International Mechanical Engineering Congress, Exposition, New York, NY, USA* pp. 1–12.

Mozurkewich, G. (1998*a*), 'Time-average temperature distribution in a thermoacoustic stack', *J. Acoust. Soc. Am.* **103**(1), 380–388.

Mozurkewich, G. (1998*b*), 'A model for transverse heat transfer in thermoacoustics', *J. Acoust. Soc. Am.* **103**(6), 3318–3326.

Mozurkewich, G. (2001), 'Heat transfer from transverse tubes adjacent to a thermoacoustic stack', *J. Acoust. Soc. Am.* **110**(2), 841–847.

Olson, J. R. & Swift, G. W. (1997), 'Acoustic streaming in pulse tube refrigerators: Tapered pulse tubes', *Cryogenics* **37**, 769–776.

Ozawa, M., Kunihiro, K. & Kawamoto, A. (1999), 'Flow visualization of acoustic streaming in a resonance tube refrigerator', *Technology Reports of Kansai University* **41**, 35–44.

Piccolo, A. & Cannistraro, G. (2002), 'Convective heat transport along a thermoacoustic couple in the transient regime', *International Journal of Thermal Sciences* **41**(11), 1067–1075.

Piccolo, A. & Pistone, G. (2006), 'Estimation of heat transfer coefficients in oscillating flows: The thermoacoustic case', *International Journal of Heat and Mass Transfer* **49**, 1631–1642.

Poese, M. E. (1998), Performance measurements on a thermoacoustic refrigerator driven at high amplitudes, Master's thesis, Pennsylvania State University Graduate School, Pennsylvania, USA.

Poese, M. E. & Garrett, S. L. (2000), 'Performance measurements on a thermoacoustic refrigerator driven at high amplitudes', *J. Acous. Soc. Am.* **107**(5), 2480–2486.

Product Information - Mylar - Physical-Thermal Properties (2003), Technical report, DuPont-Teijin Films. Virginia, USA.

Reid, R. S. (1999), Open cycle thermoacoustics, PhD thesis, Georgia Institute of Technology, USA.

Reid, R. S. & Swift, G. W. (2000), 'Experiments with a flow-through thermoacoustic refrigerator', *J. Acoust. Soc. Am.* **108**(6), 2835–2842.

Rijke, P. L. (1859), 'Notiz *ü*ber eine neue art and die in einer an beiden enden offenen röhre enthaltene luft in schwingungen zu versetzen', *Ann. Physics (Leipzig)* **107**(339).

Rivera-Alvarez, A. & Chejne, F. (2001), 'Stability analysis of thermoacoustic engines', *Journal of Non-Equilibrium Thermodynamics* **26**(1), 53–71.

Rivera-Alvarez, A. & Chejne, F. (2004), 'Non-linear phenomena in thermoacoustic engines', *Journal of Non-Equilibrium Thermodynamics* **29**(3), 209–220.

Rott, N. (1969), 'Damped and thermally driven acoustic oscillations in wide and narrow tubes', *Z. Angew. Math. Phys.* **20**, 230–243.

Rott, N. (1975), ‘Thermally driven acoustic oscillations, part III: second-order heat flux’, *Z. Angew. Math. Phys.* **26**, 43–49.

Rott, N. (1980), ‘Thermoacoustics’, *Adv. Appl. Math.* **20**, 135–175.

Schneider, T., Botta, N., Geratz, K. J. & Klein, R. (1999), ‘Extension of finite volume compressible flow solvers to multi-dimensional, variable density Mach number flows’, *Journal of Computational Physics* **155**, 248–286.

Slaton, W. V. & Zeegers, J. C. H. (2006), ‘Thermoelectric power generation in a thermoacoustic refrigerator’, *Applied Acoustics* **67**, 450–460.

Smith, B. L. & Swift, G. W. (2003), ‘Power dissipation and time-averaged pressure in oscillating flow through a sudden area change’, *J. Acous. Soc. Am* **113**(5), 2455–2463.

Smith, R. W. M., Poese, M. E., Garrett, S. L. & Wakeland, R. S. (2004), ‘Thermoacoustic device’, US Patent 6,725,670.

So, J. H., Swift, G. W. & Backhaus, S. (2006), ‘An internal streaming instability in regenerators’, *J. Acous. Soc. Am.* **120**(4), 1898–1909.

Sondhauss, C. (1850), ‘Ueber die schallschwingungen der luft in erhitzten glasröhren und in gedeckten pfeifen von ungleicher weite’, *Ann. Physics (Leipzig)* **79**(1).

Spalding, D. B. (1991), *The PHOENICS Beginner’s Guide TR100*, CHAM, Wimbledon Village, London, UK.

Sun, D., Qiu, L., Zhang, W., Yan, W. & Chen, G. (2005), ‘Investigation on travelling wave thermoacoustic heat engine with high pressure amplitude’, *Energy Conversion and Management* **46**, 281–291.

Swift, G. W. (1988), ‘Thermoacoustic engines’, *J. Acoust. Soc. Am.* **84**(4), 1145–1180.

Swift, G. W. (2002), *Thermoacoustics: A unifying perspective for some engines and refrigerators*, Acoustical Society of America, New York, USA.

Swift, G. W. & Wollan, G. (2002), Thermoacoustics for liquefaction of natural gas, *in* ‘GasTIPS’, Vol. 8, GTI.

Technologies, C. I. E. (2006), ‘Corning duratrap at filters’, Online brochure. Accessed from http://www.corning.com/docs/environmentaltechnologies/at.pdf on 28th April 2007.

Thompson, C. (1987), ‘Stability of a Stokes boundary layer’, *J. Acous. Soc. Am.* **81**(4), 861–873.

Tijani, M. E. H. (2001), Loudspeaker-driven thermo-acoustic refrigeration, PhD thesis, Eindhoven University of Technology, Netherlands.

Tijani, M. E. H., Zeegers, J. C. H. & de Waele, A. T. A. M. (2002*a*), 'Construction and performance of a thermoacoustic refrigerator', *Cryongenics* **42**, 59–66.

Tijani, M. E. H., Zeegers, J. C. H. & de Waele, A. T. A. M. (2002*b*), 'A gas spring system for optimizing loudspeakers in thermoacoustic refrigerators', *J. Appl. Physics* **92**(4), 2159–2165.

Tominaga, A. (1995), 'Thermodynamic aspects of thermoacoustic theory', *Cryogenics* **35**(427-440).

Wakeland, R. S. (2000), 'Use of electrodynamic drivers in thermoacoustic refrigerators', *J. Acoust. Soc. Am.* **107**(2), 827–832.

Wakeland, R. S. & Keolian, R. M. (2002*a*), 'Influence of velocity profile nonuniformity on minor losses for flow exiting thermoacoustic heat exchangers (l)', *J. Acous. Soc. Am.* **112**(4), 1249–1252.

Wakeland, R. S. & Keolian, R. M. (2002*b*), 'Thermoacoustics with idealized heat exchangers and no stack', *J. Acoust. Soc. Am.* **111**(6), 2654–2664.

Wakeland, R. S. & Keolian, R. M. (2004), 'Calculated effects of pressure-driven temperature oscillations on heat exchangers in thermoacoustic devices with and without a stack', *J. Acous. Soc. Am.* **116**(1), 294–302.

Ward, B. & Swift, G. W. (2001), *Design Environment for Low-Amplitude ThermoAcoustic Engines (DeltaE) Tutorial and User's Guide (Version 5.1)*, Los Alamos National Laboratory, New Mexico, USA.

Watanabe, M., Prosperetti, M. & Yuan, H. (1997), 'A simplified model for linear and nonlinear processes in thermoacoustic prime movers. Part I. Model and linear theory', *J. Acous. Soc. Am.* **102**(6), 3484–3496.

Wetzel, M. & Herman, C. (1997), 'Design optimisation of thermoacoustic refrigerators', *Int. J. Refrig.* **20**(1), 3–21.

Wetzel, M. & Herman, C. (1999), 'Experimental study of thermoacoustic effects on a single plate Part II: Heat transfer', *Heat and Mass Transfer* **35**(2), 433–441.

Wetzel, M. & Herman, C. (2000), 'Experimental study of thermoacoustic effects on a single plate Part I: Temperature fields', *Heat and Mass Transfer* **36**(1), 7–20.

Wheatley, J. C., Swift, G. & Migliori, A. (1986), 'The natural heat engine', *Los Alamos Science* **14**, 2–33. Los Alamos National Laboratory, New Mexico, USA.

Wheatley, J., Hofler, T., Swift, G. W. & Migliori, A. (1983), 'An intrinsically irreversible thermoacoustic heat engine', *J. Acous. Soc. Am.* **74**(1), 153–170.

Worlikar, A. S. & Knio, O. M. (1996), 'Numerical simulation of a thermoacoustic refrigerator. I. Unsteady adiabatic flow around the stack', *Journal of Computational Physics* **127**(2), 424–451.

Worlikar, A. S., Knio, O. M. & Klein, R. (1998), 'Numerical simulation of a thermoacoustic refrigerator. II. Stratified flow around the stack', *Journal of Computational Physics* **144**, 299–324.

Yu, G.-Y., Luo, E.-C., Dai, W., Hu, J.-Y. & Wu, Z.-H. (2006*a*), 'Study on thermodynamic and dynamic performance of thermoacoustic Stirling heat engines by using CFD Part II: Investigation on conversion characteristics from heat energy to acoustic power and gedeon acoustic stream', *Cryogenic engineering* **5**, 11–16.

Yu, G.-Y., Luo, E.-C., Dai, W., Hu, J.-Y. & Wu, Z.-H. (2006*b*), 'Thermodynamic and dynamic performance study of thermoacoustic-Stirling heat engines by using CFD Part I: Evolution process of self-excited thermoacoustic oscillation', *Cryogenic engineering* **4**, 5–9.

Yuan, H., Karpov, S. & Prosperetti, A. (1997), 'A simplified model for linear and nonlinear processes in thermoacoustic prime movers. Part II. Nonlinear oscillations', *J. Acous. Soc. Am.* **102**(6), 3497–3506.

Zhang, X. B., Qiu, L. M., Gan, Z. H. & He, Y. L. (2007), 'CFD study of a simple orifice pulse tube cooler', *Cryogenics* **47**, 315–321.

Zhou, S. & Matsubara, Y. (1998), 'Experimental research of thermoacoustic prime mover', *Cryogenics* **38**, 813–822.

List of Tables

3.1 Expanded uncertainty of measurement. 66

4.1 Flow and geometry parameters for each simulation run used in investigating blockage ratio. Run 22 only differs from Run 1 in using a mesh with grid mesh sizing equivalent to that used by Piccolo & Pistone (2006). $DR{=}|p_1|/p_m$. 79
4.2 Flow conditions and material properties used for all computational runs presented in Chapter 4. 82
4.3 Measurement points of interest. 86
4.4 Predicted $|\bar{u}_1|$, $\bar{M}_a$ and $\bar{M}$ values at Location M1 (Table 4.3) for each run. $\bar{M}_a\big|_{L_S/2}$ is found from Equation (4.9). $\bar{M}\big|_{L_S/2}$ is found from Equation (4.10). $N_{R,S}|_{L_S/2}$ values reported are maxima. 90

5.1 Grid meshes used for each modelspace in this study. Here, $\delta_\kappa/\Delta y$ is the minimum ratio of thermal penetration depth to grid mesh spacing normal to and within a distance of δ_κ from the heat exchanger surface. Refer to Figure 3.1 for definitions of the grid interval count n. e is the (spatial) ratio used within *Gambit* (*FLUENT 6.2.16 User Manual* 2006) to grade the mesh along each subdomain boundary. 113
5.2 Run number for stack plate edge shape and drive ratio. For all runs, $t_s{=}\delta_{\kappa m}{=}0.024$m, $BR{=}0.7$ at plate midlength. 116
5.3 Flow conditions and material properties used for all computational runs presented in Chapter 5. 117

6.1 Operating conditions considered in Chapter 6. All runs model helium as the working fluid. 150

B.1 Solver profiles used in this study. Refer to Sections B.1.1.1, B.1.1.2 and B.1.1.3 for specific details regarding the following settings. 189
B.2 Comparison of typical axial and lateral grid sizings used in selected numerical studies of thermoacoustic stacks: L_S is the plate length, Δx and Δy are the grid mesh spacings in the x and y directions respectively and $\delta_{\kappa m}$ is the mean thermal penetration depth. 191
B.3 Comparison of typical axial and lateral grid sizings used in this thesis. Refer to Figure 3.1 for definitions of the grid interval count n. e is the (spatial) ratio used within *Gambit* (*FLUENT 6.2.16 User Manual* 2006) to grade the mesh along each subdomain boundary. 192

B.4 Integral of time-averaged transverse heat flux $\int \langle \dot{h}_y \rangle_t dA$ (W) at limit state for various grid mesh profiles. Case files are otherwise identical to Runs 1 and 20 of Chapter 4. Using the finest grid mesh profile 'G4' as a basis, the comparative error in $\int \left\langle \dot{h}_y \right\rangle_t dA$ is also provided for each Case. 195

B.5 $\langle \Delta T_{k,hx} \rangle_t$ (K) at limit state for various grid mesh profiles. Case files are otherwise identical to Runs 1 and 20 of Chapter 4. Using the highest grid mesh density 'G4' as a basis, the comparative error in $\langle \Delta T_{k,hx} \rangle_t$ is also provided for each case. 199

B.6 Time profiles used to assess timescale dependency. Timestep (ts) size indicated for an operating frequency f of 100Hz. 202

B.7 Integral of time-averaged transverse heat flux $\int \left\langle \dot{h}_y \right\rangle_t dA$ for various timestep sizes. 203

B.8 $\langle \Delta T_{k,hx} \rangle_t$ (K) at limit state for various timestep sizes. Case files are otherwise identical to Runs 1 and 20 of Chapter 4. Using the finest time profile 'T0' as a basis, the comparative error in $\langle \Delta T_{k,hx} \rangle_t$ is also provided for each Case. 209

D.1 List of materials and operating conditions modelled in this case study. All runs model helium as the working fluid. 237

D.2 Comparison of thermophysical properties for modelling practical thermoacoustic devices. 238

List of Figures

2.1 Example of an ideal thermoacoustic heat-engine driving an ideal thermoacoustic heat-pump for an automobile air conditioner. 6

2.2 (a) Diagram of a half-wavelength thermoacoustic pump; the tube is closed at each end and an acoustic source (such as a loudspeaker) is used to pump heat; (b) Distribution of acoustic pressure and velocity amplitude along the axis of the device shown in (a); (c) Sketch of the thermodynamic cycle of a gas parcel inside the stack shown in (a); (d) Temperature versus position, and pressure versus volume for the gas parcel shown in (c). (a) and (b) adapted from Wetzel & Herman (1997), (c) and (d) adapted from Backhaus & Swift (2002). 9

2.3 Plots of pressure and velocity versus time for various thermodynamic cycles: (a) Standing Wave, showing 90° phasing between acoustic velocity and pressure; (b) Travelling Wave, showing acoustic velocity and pressure in phase; and (c) Stirling Cycle. The thermal 'delay' in standing-wave devices discussed in the text is indicated in (a). (a) and (b) adapted from Ceperley (1979), (c) adapted from Garrett & Backhaus (2000). 20

2.4 The TASHE refrigerator (reproduced with permission from Swift (2002, p23)). ©The Acoustical Society of America. 21

2.5 Diagram showing the evolution of the 'streamfunction' distribution, reproduced from Worlikar & Knio (1996, Fig. 3). Time interval between each figure is 45° shown with reference to the acoustic velocity (arrows to left of each diagram). ©Elsevier Limited. 33

2.6 Computational domains (boundaries indicated by broken line) used by (a), (b) Ishikawa & Mee (2002, Figure 1) and (c) Piccolo & Pistone (2006). 36

2.7 Experimental PIV (top row) and numerically predicted (bottom row) results of instantaneous velocity vectors and vorticity contours at selected timeframes at the cold end of a thermoacoustic stack (Reproduced with permission from Blanc-Benon et al. (2003, p22)). ©Comptes rendus Mécanique. 46

3.1 Annotated sketch of the thermoacoustic couple modelspace. Shaded areas are regions of solid material. Dimensions of axial length are denoted by L, transverse length scales by y. n_{xS} and n_{yS} describe the number of mesh subdivisions in the x and y directions respectively for domain S. 59

3.2 Fluent *6.2.16* typical screen output of scaled residuals over 5 time steps. 64
3.3 Experimental standard deviation of the mean (ESDM) of the time-averaged heat flux across the heat exchanger surface S, $\langle \dot{h}_S \rangle_t$. The ESDM result for vertical edge surfaces at each end of the plate are highlighted. 65

4.1 Region of the computational domain within the basic theoretical model of half-wavelength resonator tube with parallel plate stack. The acoustic source is located at the left end of the computational domain (not shown). 74
4.2 Comparison of computational domains used by (a) Ishikawa & Mee (2002), (b) Piccolo & Pistone (2006) and (c) this study. (d) a closer view of the stack region shown in (c). 75
4.3 Computational domains used in this study showing boundary conditions and selected geometry. (b) a closer view of the stack region shown in (a). 77
4.4 p_1, u_1 and $\Delta T_{k,hx}$ (Section 4.1.5.1) at the oscillatory boundary (INLET) versus simulation timesteps 0 to 1000 and 1900 to 2100 for Run 6. Positive velocity is to the right with reference to Figure 4.3. 84
4.5 Temperature versus specific entropy for position at the midspacing and the midlength of the stack region ($x = L_S/2$, $y = 0$) over the first ten cycles of Run 1. Points of interest are marked for time steps 0017 (flow-time 0.0017s), 0076 (flow-time 0.0076s) and 0176 (flow-time 0.0176s). 85
4.6 Diagram indicating measurement points of interest listed in Table 4.3. Diagram is not to scale. 87
4.7 Estimated distribution of mean and RMS velocity magnitude along the mid-plate line (y=0), for the time period 0.2000s to 0.2100s. Data shown is for Run 20, with BR=0.7 and DR=6.8%. 89
4.8 Flow pathlines for Run 20, at (a) t=0.200s, (b) t=0.201s, (c) t=0.202s, (d) t=0.203s, (e) t=0.204s. The prevailing flow direction and velocity magnitude are indicated to the left of each figure. Pathlines are coloured by velocity magnitude as indicated by the scale at the bottom of the figure. 92
4.9 Flow pathlines for Run 20, at (a) t=0.205s, (b) t=0.206s, (c) t=0.207s, (d) t=0.208s, (e) t=0.209s. The prevailing flow direction and velocity magnitude are indicated to the left of each figure. Pathlines are coloured by velocity magnitude as indicated by the scale at the bottom of the figure. 93
4.10 Rate of entropy generation $\dot{S}_{\text{gen}}$ versus drive-ratio DR, with selected runs grouped by blockage ratio, as follows: BR=1.0 (Runs 1 to 4), BR=0.98 (Runs 5 to 8), BR=0.9 (Runs 9 to 12), BR=0.8 (Runs 13 to 16), BR=0.7 (Runs 17 to 21). The analytical result of Swift was generated from use of Equation 89 of Ref. (Swift 1988). 95

4.11 Distribution of time-averaged heat flux in the y-direction $\left\langle \dot{h}_y \right\rangle_t$ along the horizontal plate surface according to axial position x. Open circles are approximate numerical data from the study of Piccolo & Pistone (2006, Run 1). Positive $\dot{h}_y$ indicates net heat transfer from the plate to the working fluid. 97

4.12 Temperature versus entropy cycles at limit state for Run 1 for selected fixed positions defined in Table 4.3. The position and direction of the cycle at the 2000th time step (flow time 0.2s) is indicated with a solid arrow. Phases of maximum and minimum pressure are indicated for locations C2, M2 and H2. 99

4.13 Limit state behaviour of temperature versus entropy for Runs 4 and 20 at Locations C1, M1 and H1. 100

4.14 Surface plot of normalised transverse heat flux $\dot{h}_y$ (Appendix C.1) through the horizontal plate surface for the limit state cycle of Run 1. Surface colour mapping indicates positions of cooling (blue) and heating (red). 101

4.15 Surface plot of normalised transverse heat flux $\dot{h}_y$ (Appendix C.1) through the horizontal plate surface for the limit state cycle of Run 20. Note the difference z-axis scaling to Figure 4.14. Surface colour mapping indicates positions of cooling (blue) and heating (red). . . . 102

4.16 Sketch showing the proportion of time-averaged heat flux through the plate surface for limit-state operation of Run 20. Percentage values quoted are referenced to the total heat flux entering the plate over an oscillatory cycle, $\langle \dot{h}_{hx} \rangle_t |_{cold}$. 104

4.17 Time-averaged transverse heat flux for DR=6.8% and increasing BR. Data shown is for Run 4 (t_s =0), Run 8 (t_s =0.16mm), Run 12 (t_s =0.8mm), Run 16 (t_s =1.6mm) and Run 20 (t_s =2.4mm). 104

4.18 Time-averaged transverse heat flux for BR=0.7 and increasing DR. Data shown is for Run 17 (DR=1.7%), Run 18 (DR=3.4%), Run 19 (DR=5.1%) and Run 20 (DR=6.8%). 105

4.19 Time-averaged difference in area-weighted average gas temperature normalised by same result obtained using a blockage ratio BR of 1 (Runs 1 to 4) versus drive-ratio DR. Data is presented from Runs 5 to 8 (BR=0.98), Runs 9 to 12 (BR=0.9), Runs 13 to 16 (BR=0.8) and Runs 17 to 20 (BR=0.7). 106

5.1 Sketches of modelspaces used for modelling different stack end shapes: (a) zero-thickness plates (Ishikawa 1999, Cao et al. 1996), (b) Rectangular (Finite thickness), (c) Rounded edges, (d) Bulbous edges, (e) Talon edges and (f) Aerofoil edges. All modelspaces shown are otherwise identical to that presented in Figure 4.2(c). The thickness of all plates in the centre of the stack region, t_s, is equal to the mean thermal penetration depth $\delta_{\kappa m}$. 111

5.2 Close-up view of the grid meshes for (a) Rectangular, (b) Rounded, (c) Bulbous, (d) Talon and (e) Aerofoil edge shape models at the 'cold' end of the stack region ($x \sim 0$). All five meshes shown are at the relative scale indicated. 115
5.3 Example normal unit vector $\hat{\mathbf{n}}$ to the heat exchanger surface S. 118
5.4 Diagram of a thermoacoustic couple with arbitrarily shaped heat exchanger surface S. 119
5.5 Arrangement and parameters used to determine the acoustic power $\dot{E}_2$ within the *Fluent* CFD environment, using pressure p_i and volume velocity U_i obtained at the ith segment of boundary 'INLET'. 121
5.6 Pathlines coloured by velocity magnitude for (a) Rectangular (Run 1), (b) Rounded (Run 2), (c) Bulbous (Run 3), (d) Talon (Run 4) and Aerofoil (Run 5) edge shape profiles at time t=0.2s. DR=1.7%. 126
5.7 Pathlines coloured by velocity magnitude for (a) Rectangular (Run 11), (b) Rounded (Run 12), (c) Bulbous (Run 13), (d) Talon (Run 14) and Aerofoil (Run 15) edge shape profiles at time t=0.2s. DR=5.1%. 127
5.8 Flow pathlines for Run 4, DR=1.7%, at (a) t=0.200s, (b) t=0.201s, (c) t=0.202s, (d) t=0.203s and (e) t=0.204s. The prevailing flow direction and velocity magnitude are indicated to the left of each figure. 128
5.9 Flow pathlines for Run 4, DR=1.7%, at (a) t=0.205s, (b) t=0.206s, (c) t=0.207s, (d) t=0.208s and (e) t=0.209s. The prevailing flow direction and velocity magnitude are indicated to the left of each figure. 129
5.10 Surface plot of normalised heat flux $\dot{h}_S$ for the Rounded stack plate profile using a drive ratio of 1.7% (Run 2). 131
5.11 Annotated surface plot of normalised heat flux $\dot{h}_S$ for the Talon stack plate profile using a drive ratio of 1.7% (Run 4). (△) indicates the range of heat flux attributed to the rounded surface on the cold side of the stack plate. (◇) indicates the range of heat flux attributed to the vertical internal surface on the left side of the stack plate. ($*$) indicates the additional heat transfer at the 'hot end' of the stack due to the 'secondary' recirculation zone which develops on the inside of the stack edge. 132
5.12 Surface plot of normalised heat flux $\dot{h}_S$ for the Aerofoil stack plate profile using a drive ratio of 1.7% (Run 5). 133
5.13 Time-averaged heat flux across the stack plate surface $\langle \dot{h}_{hx} \rangle_t$ (normalised using rectangular edge shape result) versus $\dot{E}_2$ normalised by the result of Run 1. Four points of increasing DR (left to right) are plotted for each edge shape modelled. 134
5.14 Distribution of time-averaged heat flux across the stack plate surface $\langle \dot{h} \rangle_t$ for normalised axial position x/L_S for a drive ratio of 1.7% (Runs 1 to 5). 135
5.15 Distribution of time-averaged heat flux across the stack plate surface $\langle \dot{h} \rangle_t$ for normalised axial position x/L_S for a drive ratio of 6.8% (Runs 15 to 20). 135

5.16 Distribution of time-averaged heat flux as per Figure 5.14 showing increased detail near the 'cold' end of the thermoacoustic couple. Runs 1 to 5 shown (DR of 1.7%). Distortions in $\langle \dot{h} \rangle_t$ due to sudden bends in the shapes of the Talon and Bulbous modelspaces are highlighted ($*$). 136

5.17 Distribution of time-averaged heat flux as per Figure 5.15 showing increased detail near the 'cold' end of the thermoacoustic couple. Runs 15 to 20 shown (DR of 6.8%). Distortions in $\langle \dot{h} \rangle_t$ due to sudden bends in the shapes of the Talon and Bulbous modelspaces are highlighted ($*$). 136

5.18 Sketch indicative of time-averaged heat flux $\langle \dot{h}_{hx} \rangle_t$ (W/m^2) across the cold end of Run 4 (Talon edge). Drive ratio is 1.7%. 137

5.19 Sketch indicative of time-averaged heat flux $\langle \dot{h}_{hx} \rangle_t$ (W/m^2) across the cold end of Run 19 (Talon edge). Drive ratio is 6.8%. 137

5.20 Effective cooling power $\dot{Q}_{S,\mathrm{cold}}$ (normalised using rectangular edge shape result) versus normalised $\dot{E}_2$. 139

5.21 Coefficient of performance COP versus drive ratio for all edge shape profiles considered in this study. 140

5.22 Normalised $\Delta T_{k,hx}$ versus drive ratio for various edge shape conditions. 141

5.23 Time-averaged gas temperature T_k for the Rectangular edge shape model versus axial position normalised by stack length for drive ratios 1.7% (Run 1) to 6.8% (Run 16). The stack plate edges are marked with vertical lines at x/L_S equal to 0 and 1. 142

5.24 Time-averaged gas temperature $\langle T_k \rangle_t$ versus axial position normalised by stack length for selected edge shape conditions. Runs 1 to 5 are presented for which the drive ratio is common and equal to 1.7%. . . 143

5.25 Time-averaged gas temperature $\langle T_k \rangle_t$ versus axial position normalised by stack length for selected edge shape conditions. Runs 11 to 15 are presented for which the drive ratio is common and equal to 5.1%. . . 143

6.1 Sketch of the computational domain of the expanded thermoacoustic couple model within a half wavelength standing-wave resonator. . . . 148

6.2 Sketch of boundary conditions and major geometry features of the expanded thermoacoustic couple model. 149

6.3 Distribution of streaming Reynolds number $N_{R,S}$ at t=0.21s using a drive ratio of (a) 1.7% (Run 2) and (b) 5.1% (Run 4). p_m= 1 bar. . . 152

6.4 Pathlines for the (a) left stack plate ends for Run 4, (b) left end of Run 5 of Appendix D.3, and (c) right stack plate ends for Run 4, t=0.21s. Pathlines are coloured by velocity magnitude (m/s). Stack plate numbers are annotated. 153

6.5 Comparison of pathlines on the right end of Runs 3 (left) and 4 (right). Phase is (a) ϕ=0°, (b) ϕ=18°, (c) ϕ=36°, (d) ϕ=54° and (e) ϕ=72°. Free stream velocity direction and magnitude are indicated on the right of each figure. 156

6.6 Comparison of pathlines on the right end of Runs 3 (left) and 4 (right). Phase is (a) ϕ=90°, (b) ϕ=108°, (c) ϕ=126°, (d) ϕ=144° and (e) ϕ=162°. Free stream velocity direction and magnitude are indicated on the right of each figure. 157
6.7 Mean x velocity $\langle u \rangle_t$ for (a) Run 1, (b) Run 17 of Chapter 4 (result mirrored across stack plate mid-thickness), (c) Run 3 and (d) Run 4. Areas not coloured (white) are outside the range -4 to 4 m/s. Positive $\langle u \rangle_t$ is to the right of figure. 160
6.8 Mean x velocity $\langle u \rangle_t$ for Run 4, showing entire stack region. Areas not coloured (white) are outside the range -6 to 6 m/s. Positive $\langle u \rangle_t$ is to the right of figure. 161
6.9 Normalised mean x velocity versus normalised y position on line of stack midsection (x=$L_S/2$) for Runs 3 to 5 ($t_s/\delta_{\kappa m}$=3.2). Positive $\langle u \rangle_t/u_{rms}$ is rightward. Labelled grey shaded areas represent each of the four stack plates. 163
6.10 Normalised mean x velocity versus normalised y position on line of stack midsection (x=$L_S/2$), for Runs 6 to 8 ($t_s/\delta_{\kappa m}$=1.0). Positive $\langle u \rangle_t/u_{rms}$ is rightward. Labelled grey shaded areas represent each of the four stack plates. 164
6.11 Distribution of the time-averaged heat flux for all four plates of Run 1 and Run 1 of Chapter 5. Mean pressure p_m is 0.1 bar. 165
6.12 Distribution of the time-averaged heat flux as per Figure 6.11 showing increased detail on the 'cold' end of the thermoacoustic couple / stack region. 166
6.13 (a) Distribution of time-averaged heat flux in the y-direction $\left\langle \dot{h}_y \right\rangle_t$ along the horizontal plate surface according to axial position x for Run 3. p_m=1 bar, DR=1.7%. (b) Increased detail of (a) near the 'cold end of the stack. 167
6.14 (a) Distribution of time-averaged heat flux in the y-direction $\left\langle \dot{h}_y \right\rangle_t$ along the horizontal plate surface according to axial position x for Run 4. p_m=1 bar, DR=3.4%. (b) Increased detail of (a) near the 'cold end of the stack. The arithmetic average of both upper and lower sides of Stack Plate 4, and the arithmetic average of the lower surface of Stack Plate 3 and upper surface of Stack Plate 4 are also plotted. 168
6.15 Contours of mean temperature for increasing drive ratio. (a) Run 3, DR=1.7%, (b) Run 4, DR=3.4%, (c) Run 5, DR=5.1%. 170
6.16 COP for normalised acoustic power input using the results of Runs 3 to 8. 171

B.1 Normalised error of total system states versus acoustic cycle for Run 1 of Chapter 4. Pressure states are evaluated near the cold side of the stack. 183

B.2 Velocity magnitude colour vector plot from the *Fluent* CFD environment about the left edge of the thermoacoustic couple simulated in Run 20 of Chapter 4, at t=0.2s. Prevailing flow direction is left to right: contours are shown for the range 0 to 70m/s. 184
B.3 Time-averaged transverse heat flux versus normalised stack position for selected solver profiles. Modelspace is of a thermoacoustic couple of zero thickness using a 133,000 node mesh. DR of 1.7%. 190
B.4 Close-up view of grid meshes using profiles (a) G2, (b) G3, (c) G4 and (d) G5. 194
B.5 Normalised stack position x/L_S versus time-averaged transverse heat flux $\left\langle \dot{h}_y \right\rangle_t$ for Case A using selected grid mesh profiles. 197
B.6 Close up of Figure B.5 for the range x/L_S=0 to 0.15. 197
B.7 Normalised stack position x/L_S versus time-averaged transverse heat flux $\left\langle \dot{h}_y \right\rangle_t$ for Case B using selected grid mesh profiles. 198
B.8 Close up of Figure B.7 for the range x/L_S=0 to 0.15. 198
B.9 Normalised stack position x/L_S versus time-averaged transverse heat flux $\left\langle \dot{h}_y \right\rangle_t$ for the stack 'cold end' in Case A using selected timescale profiles. 204
B.10 Normalised stack position x/L_S versus time-averaged transverse heat flux $\left\langle \dot{h}_y \right\rangle_t$ for the stack 'hot end' in Case A using selected timescale profiles. 204
B.11 Normalised stack position x/L_S versus time-averaged transverse heat flux $\left\langle \dot{h}_y \right\rangle_t$ for the stack midsection in Case A using selected timescale profiles. 205
B.12 Normalised stack position x/L_S versus time-averaged transverse heat flux $\left\langle \dot{h}_y \right\rangle_t$ for the stack midsection in Case B using selected timescale profiles. 205
B.13 Normalised stack position x/L_S versus time-averaged transverse heat flux $\left\langle \dot{h}_y \right\rangle_t$ for the stack 'cold end' in Case B using selected timescale profiles. 206
B.14 Normalised stack position x/L_S versus time-averaged transverse heat flux $\left\langle \dot{h}_y \right\rangle_t$ for the stack 'hot end' in Case B using selected timescale profiles. 206
B.15 $\Delta T_{k,hx}$ versus time for Case A with selected timescale profiles. 207
B.16 $\Delta T_{k,hx}$ versus time for Cases A and B with selected timescale profiles. 208
B.17 Normalised difference in time-averaged gas temperature on y=0 versus axial position x for Run 19. The experimental result of Kawamoto et al. (1998, Figure 10) is provided for comparison. 213
B.18 Difference in temperature maxima and minima on y=0 versus simulation time t. 214

C.1 Example of a surface contour plot showing the evolution of transverse heat flux $\dot{h}_y$ over the surface of a thermoacoustic couple. Data is shown for Run 20 of Chapter 4. 221
C.2 Surface contour plot of $\dot{h}_S$ from Run 17 of Chapter 5, without (a) and with (b) removal of bulk gas compression effects. 222
C.3 Surface plot of temperature along y=0 for Run 5 of Chapter 5, t 0.2s to 0.21s. Plot is normalised by the temperature at (0,0.126m) to remove bulk gas compression effects. 223

D.1 Sketch of *DeltaE* segment arrangement and overall dimensions. 229
D.2 COP versus drive ratio DR as calculated using the higher order model (Runs 4, 5, 6 of Chapter 6 and Run 5 of Section D.3) and the linear prediction tool *DeltaE*. p_m=1 bar. 230
D.3 $\dot{E}_2/y_0$ versus drive ratio DR as calculated using the higher order model (Runs 4, 5, 6 of Chapter 6 and Run 5 of Section D.3) and the linear prediction tool *DeltaE*. 230
D.4 Evolution of temperature contours over a complete oscillatory cycle ('Hot' end shown with image horizontally reversed and mirrored across y=0 for comparison with Wetzel & Herman (2000, Figure 3)). Phase is (a) ϕ=0°, (b) ϕ=36°, (c) ϕ=72°, (d) ϕ=108°, (e) ϕ=144°, (f) ϕ=180°, (g) ϕ=216°, (h) ϕ=252°, (i) ϕ=288°, and (j) ϕ=324°. Flow direction is indicated at the left of each figure. 233
D.5 Evolution of flow pathlines over a complete oscillatory cycle ('Hot' end shown with image horizontally reversed and mirrored across y=0 for comparison with Figure D.4). Phase is (a) ϕ=0°, (b) ϕ=36°, (c) ϕ=72°, (d) ϕ=108°, (e) ϕ=144°, (f) ϕ=180°, (g) ϕ=216°, (h) ϕ=252°, (i) ϕ=288°, and (j) ϕ=324°. Flow direction is indicated at the left of each figure. 234
D.6 Visualisation of the flow field at the edges of the stack plates for the drive ratios (a) DR=1% and (b) DR=3%. (c) Schematic of the edge effects at the stack plates (Reproduced with permisson (Wetzel & Herman 2000, Figure 3)). ©Springer-Verlag 2000. 235
D.7 Evolution of the vorticity field for case 6 of Worlikar & Knio (1996), using 45° phase increments, i.e. (a) t=32π/4, (b) t=33π/4, (c) t=34π/4, (d) t=35π/4, (e) t=36π/4, (f) t=37π/4, (g) t=38π/4, and (h) t=39π/4 (Reproduced with permisson (Worlikar & Knio 1996, Figure 8)). ©Elsevier Limited. 236
D.8 Cooling power $\dot{Q}_{s,cold}$, $\dot{E}_2$, COP and COP_r for each material normalised by result obtained using Run 6. 242

‘Animations DVD’ is available in the University of Adelaide Library.